Lattice-Matched (In,Ga)P Buffer Layers for ZnSe Based Visible Emitters

by

Kan Lu

Submitted to the Department of Electrical Engineering and Computer Science
in partial fulfillment of the requirements for the degree of

Master of Science in Electrical Engineering and Computer Science

at the

MASSACHUSETTS INSTITUTE OF TECHNOLOGY

February 1994

© Massachusetts Institute of Technology 1994. All rights reserved.

Author ....
Department of Electrical Engineering and Computer Science
February 16, 1994

Certified by ....
Leslie A. Kolodziejski
Associate Professor
Thesis Supervisor

Accepted by ....
Frederic R. Morgenthaler
Chairman, Departmental Committee on graduate Students

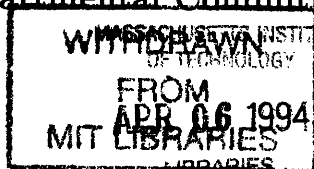

Lattice-Matched (In,Ga)P Buffer Layers for ZnSe Based Visible Emitters

by

Kan Lu

Submitted to the Department of Electrical Engineering and Computer Science
on February 16, 1994, in partial fulfillment of the
requirements for the degree of
Master of Science in Electrical Engineering and Computer Science

Abstract

This research project is to study the growth of (In,Ga)P buffer layers lattice-matched to ZnSe. Both ZnSe and (In,Ga)P were grown by gas source molecular beam epitaxy. The ZnSe layers were grown using elemental Zn and thermally decomposed H_2Se. The II-VI nucleation occurred following an *ex situ* transfer in air of the As-passivated (In,Ga)P buffer layers, grown using In, Ga, and cracked PH_3. Microstructural characterization of the II-VI/III-V heterostructures was performed with high resolution x-ray diffraction and transmission electron microscopy. The (511) reflection of the x-ray rocking curve was used to measure the residual strain in the ZnSe/(In,Ga)P/GaAs structures, and to determine the alloy composition of the (In,Ga)P. The (400) reflection of the x-ray diffraction rocking curves indicated full-width-at-half-maximum of 130 arcseconds and 18 arcseconds for the relaxed ZnSe on thin (1 μm) pseudomorphic (In,Ga)P buffer layers, respectively. Thick (> 4 μm) partially relaxed (In,Ga)P buffer layers show cross hatch on the surface. Low temperature photoluminescence spectra originating from the ZnSe films on the (In,Ga)P buffer layers were dominated by donor-bound and free excitonic features with each exhibiting nearly the same intensity. (In,Ga)P photoluminescence was also studied.

Thesis Supervisor: Leslie A. Kolodziejski
Title: Associate Professor of Electrical Engineering

Acknowledgments

Without the scientific, technical, and moral supports of many other people this thesis as well as a wonderful graduate study at MIT would be impossible.

First and foremost, I owe enormous debt to my thesis advisor, Professor Leslie Kolodziejski. Under her supervision I have learned to appreciate and enjoy research. Her patience in teaching, and enthusiasm about science always inspired me to explore for the truth. I would also like to thank Dr. Gale Petrich for introducing me the wonderful world of molecular beam epitaxy.

A special thanks to Jay Damask for the wonderful time during our collaboration. We did most of the growth and analysis together. Other members in MIT CBE group have contributed greatly to my study: Eason Ho, Chris Coronado and Philip Fisher have grown all the ZnSe films, and Jody House performed all the photoluminescence measurement. I own a great deal of debt to them.

Finally, I would like to thank my dear mother and father. It is my parents who encouraged me and made what I am. They led me into the arena of science when I was only a child and taught me that the scientific knowledge is the most valuable thing in the world. Without their firm belief in me and huge support, I would not to make it in MIT. They deserve my deepest appreciation.

Contents

1 Introduction **10**

2 Epitaxial Growth **17**

2.1 Gas Source Molecular Beam Epitaxy 17

2.2 Reflection High Energy Electron Diffraction 25

2.3 Growth Procedure 33

2.3.1 Substrate Preparation 33

2.3.2 (In,Ga)P Growth 35

2.4 ZnSe Growth Procedure 36

3 Critical Thickness **38**

3.1 Force-Balancing Model 38

3.2 Energy-Balancing Model 41

3.3 Discussion 42

4 X-ray Characterization **46**

4.1 Structural Characterization of (In,Ga)P 48

4.2 X-ray Diffraction Measurement of (In,Ga)P Buffer Layer 54

5 Structural and Optical Characterization of ZnSe on (In,Ga)P **60**

6 Summary **37**

List of Figures

1-1 III-V and II-VI semiconductor bandgap energy versus lattice parameter diagram. 11

1-2 Epitaxial laser consists of a Zn(Te,Se) graded contact layer, Zn(S,Se) cladding layers, ZnSe/(Zn,Cd)Se quantum well(s), a GaAs buffer layer, and the GaAs substrate [16]. 12

1-3 ZnSe/(Zn,Mg)(S,Se) blue laser diode structure showing (Zn,Mg)(S,Se) cladding layers, (Zn,Mg)(S,Se)/ZnSe multiquantum well(s) on a Si-doped n-type GaAs substrate [22]. 13

1-4 The energy band lineup of ZnSe/InGaP/GaAs heterostructure. 15

2-1 Schematic layout of the principal components of the II-VI and III-V gas source molecular beam epitaxy system. 18

2-2 Schematic diagram of the GSMBE system utilized for the growth of p- and n-type (In,Ga)P and other III-V compound semiconductors. . . . 20

2-3 The experimental Ga flux versus temperature diagram and its theoretical fit using Eq.2.3. 22

2-4 In and Ga flux transition during the initial 5 minutes after the substrate shutter is opened. The lines are drawn to guide the eye. 23

2-5 The In flux measured by a flux ion gauge over a period of six months. 24

2-6 Nomarski interference optical micrograph showing a typical density of irregular shaped hilllocks or pits [26]. 25

2-7 Scanning electron microscope image showing a detailed view of an oval defect. The ridge of the defect is approximately 0.2 μm high [27]. . . 26

2-8 A schematic diagram of a typical RHEED setup contained in a molecular beam epitaxy system. 27
2-9 Electron beam penetrates the sample at a very small angle. Although the beam travels a long distance (~ several mm) inside the sample, the effective penetration depth is very small (~ 10-20 Å). 28
2-10 The RHEED reconstruction pattern of the GaAs substrate observed at 580°C. 29
2-11 The RHEED reconstruction pattern of the GaAs substrate observed at 620°C. 30
2-12 In the layer-by-layer growth mode, epitaxial growth proceeds in a two-dimensional manner, with the completion of one monolayer before the next monolayer begins to grow. 31
2-13 A typical GaAs RHEED intensity oscillation measurement with a growth rate of 0.39 μm/hour. 32
2-14 A typical (In,Ga)P RHEED intensity oscillation measurement with a growth rate of 0.8 μm/hour 32
2-15 The growth rate measured from (In,Ga)P RHEED intensity oscillations decreases over time from the start of the growth. 33
2-16 GaAs RHEED intensity oscillation obtained by closing the AsH_3 shutter for a very short time (~ 1 second) during the growth followed by resuming the GaAs growth. 34
2-17 (In,Ga)P RHEED intensity oscillation obtained at the beginning of an (In,Ga)P growth; the oscillations last for over 5 minutes. 35

3-1 Forces applied on an epitaxial layer A on a lattice-mismatched substrate B. 40
3-2 Cross-sectional high resolution transmission electron micrograph of an (In,Ga)P buffer layer on a GaAs substrate [36]. 40
3-3 The critical thickness versus composition x in $In_{1-x}Ga_xP$ calculated from the force-balancing model and the energy-balancing model. . . . 42

3-4 The critical thickness under tensile and compressive strain evaluated from energy-balancing model. 45

4-1 Schematic illustration of the x-ray diffraction mechanism 47

4-2 Schematic illustration of a double crystal x-ray diffraction measurement setup 47

4-3 Schematic illustration of the tilt which develops for a mismatched and tetragonally-distorted coherent epitaxial layer grown on a stepped surface 49

4-4 The misorientation angle between epitaxial layer and substrate Bragg planes for the case of a coherent and tetragonally distorted epitaxial layer. 51

4-5 Glancing exit and glancing incidence for an asymmetric x-ray reflection. 52

4-6 Bede x-ray setup and the relationships between the angles of first crystal, second crystal and the detector. 53

4-7 A typical (400) double crystal x-ray diffraction rocking curve for a 1 μm pseudomorphic (In,Ga)P layer on the GaAs substrate. The peak separation between (In,Ga)P and GaAs is 328 arcseconds. 54

4-8 The (400) and (511) double crystal x-ray diffraction rocking curves for a partially-relaxed (In,Ga)P film. 55

4-9 Interference optical micrograph of a partially-relaxed (In,Ga)P on GaAs substrate showed cross hatching patterns along [100] and [010] directions 56

4-10 The (400) double crystal x-ray diffraction rocking curve of (In,Ga)P having a FWHM of 34 arcseconds.. 57

4-11 The (400) double crystal x-ray diffraction rocking curve of (In,Ga)P having a FWHM of 18 arcseconds.. 57

4-12 FWHM of (In,Ga)P x-ray rocking curves versus lattice mismatch between (In,Ga)P and GaAs substrate. 58

4-13 (In,Ga)P lattice relaxation versus Ga composition for (In,Ga)P epitaxial layers 59

5-1 The (400) rocking curve of 1.9 μm ZnSe/1.15 μm $In_{0.5}Ga_{0.5}P$/GaAs heterostructure. The FWHM of the ZnSe is 130 arcseconds. 61
5-2 The (400) rocking curve of the 1.15 μm $In_{0.5}Ga_{0.5}P$ heterostructure having a FWHM of 18 arcseconds. 62
5-3 TEM image of 2 μm ZnSe/1 μm (In,Ga)P heterostructure [36]. 62
5-4 TEM image of the interface between 4 μm $In_{0.56}Ga_{0.44}P$ and the GaAs substrate [36]. 63
5-5 The (400) x-ray rocking curve of a 4 μm partially-relaxed (In,Ga)P on GaAs substrate 64
5-6 The 10K photoluminescence spectrum from a 1.1 μm ZnSe/4.3 μm $In_{0.52}Ga_{0.48}P$/GaAs heterostructure. A 0.11% lattice-mismatch still remains between the ZnSe layer and the (In,Ga)P buffer layer. 65
5-7 A typical PL spectrum plot for (In,Ga)P grown on the GaAs substrate. 65
5-8 Bandgap energy versus % Ga for 4 μm (In,Ga)P films with a least square fit. 66

List of Tables

2.1 Principle components and their functions in a MBE system 20

2.2 Degreasing procedure for GaAs substrates 34

Chapter 1

Introduction

While long wavelength light emitting devices and semiconductor lasers have been successfully developed in the past several decades [1, 2, 3, 4, 5, 6, 7], the light emitting devices and lasers operating in the visible wavelength, particularly in the blue/green region, have remained to be a major challenge. Blue/green light emitters require a material with a direct bandgap energy above 2.5 eV, but most of the III-V materials' bandgap energies are below 2.4 eV. A natural candidate is ZnSe, ZnS and their related II-VI materials with bandgap energies above 2.5 eV (Fig. 1-1). However, it is extremely difficult to produce low resistivity p-type II-VI materials. Conventional nitrogen doping, as well as P and As doping, by molecular beam epitaxy were unsuccessful in obtaining p-type conductivity [8, 9]. Although Li doping can achieve a net hole concentration of 1×10^{17} cm^{-3}, its high diffusion coefficient limits the material's stability [10, 11]. It was only until recently that the p-doping difficulty was overcome by using a nitrogen plasma source made by Oxford Applied Research [12]. Net hole carrier concentration of 10^{17} to 10^{18} have been achieved [12, 13, 14]. The successful p-type doping of ZnSe has led to the development of p-n junction light emitting diodes and semiconductor lasers operating in the blue and blue/green wavelength [15, 16, 17, 18].

Most devices to date have been employing carrier injection at a p-n junction. The active region is based on (Zn,Cd)Se/Zn(S,Se) multiple quantum well (MQW) structures. Carrier movement is limited by its diffusion length, which is typically

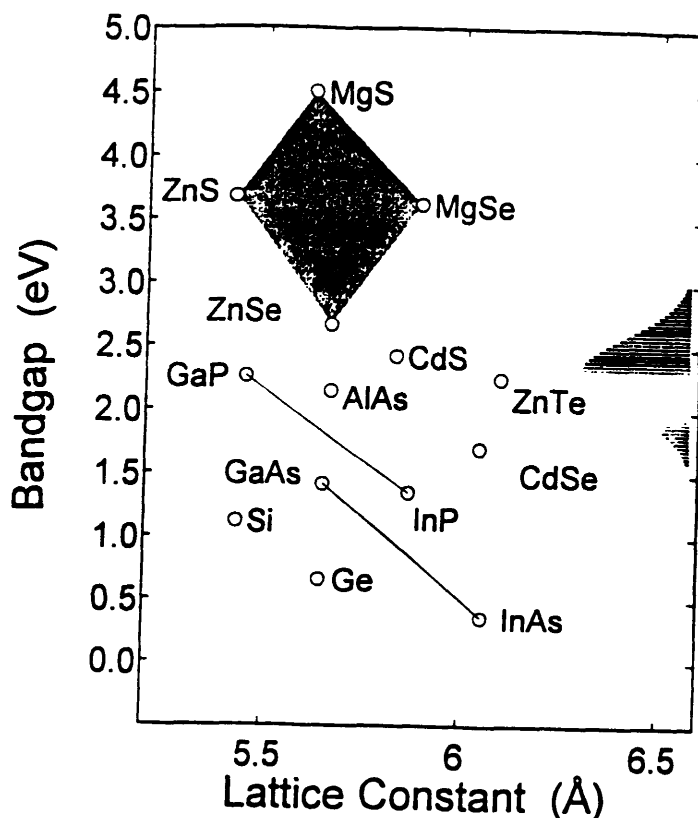

Figure 1-1: III-V and II-VI semiconductor bandgap energy versus lattice parameter diagram.

much larger than the quantum well width. The carriers in a quantum well structure are confined to a much smaller region in contrast to the case for the homojunction devices. Therefore, the multiple quantum well structure significantly increases the quantum efficiency and thus decreases the threshold current density. (Zn,Mg)(S,Se) is considered to be the best candidate for cladding layers because of its higher bandgap which can form a reservoir to confine carriers.

II-VI materials and light emitting devices have experienced great advancement in the past several years. But there are still many obstacles remaining before any commercially viable devices can be made. One of the remaining material challenges is to minimize misfit dislocations in the ZnSe and its related II-VI compounds. ZnSe has a lattice constant of 5.6676Å. Unlike III-V materials, it is difficult to grow a bulk ZnSe crystal with low dislocation density. Although recent results showed that a dislocation density of $10^5/cm^3$ is obtained for ZnSe substrates, the doping of bulk ZnSe still remains a serious problem. A semi-insulating substrate will prevent the conventional

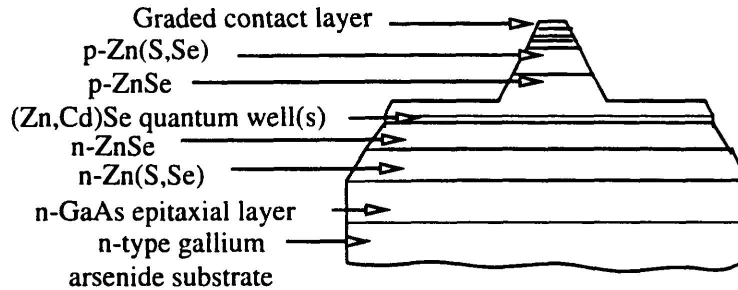

Figure 1-2: Epitaxial laser consists of a Zn(Te,Se) graded contact layer, Zn(S,Se) cladding layers, ZnSe/(Zn,Cd)Se quantum well(s), a GaAs buffer layer, and the GaAs substrate [16].

backside contact method and force the use of a side contact which could severely increase the contact resistance and increase the turn-on voltage. For these reasons, the majority of the II-VI devices use GaAs as their substrates. GaAs substrate has the advantage that (i) it is very closely lattice-matched to ZnSe with a mismatch of only 0.25 percent, (ii) its dislocation density is below $10^5/cm^3$, and (iii) the cost is relatively cheap. Furthermore, it also provides the opportunity of integrating III-V and II-VI devices onto a single chip, such as integrating a III-V laser driver circuit to drive a II-VI laser. The problem with using the GaAs substrate is that experimental results indicate that the critical thickness for a ZnSe layer grown on GaAs is only about 150 nm [19]. There are significant misfit dislocations introduced into the ZnSe epitaxial layer if the film's thickness is beyond the critical thickness. A typical laser diode structure is 2 to 3 μm thick which is far beyond the critical thickness of ZnSe. It has been shown that the density of dislocations in ZnSe generated by mismatch during film growth could be as high as or above $10^8/cm^3$ [20]. The high density of misfit dislocations greatly degrades the optical and electrical properties of II-VI devices.

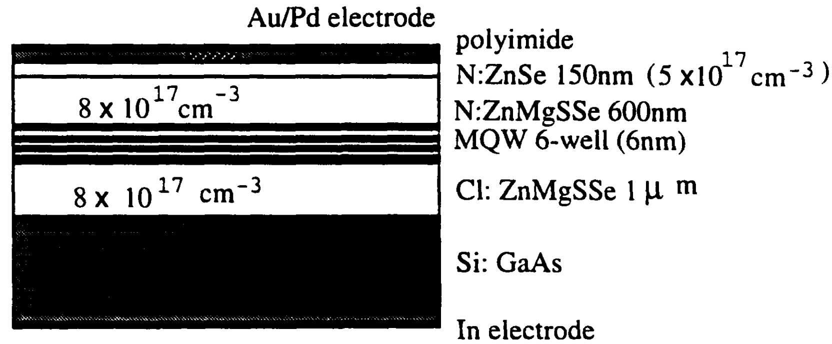

Figure 1-3: ZnSe/(Zn,Mg)(S,Se) blue laser diode structure showing (Zn,Mg)(S,Se) cladding layers, (Zn,Mg)(S,Se)/ZnSe multiquantum well(s) on a Si-doped n-type GaAs substrate [22].

One method to reduce the dislocation density in II-VI epitaxial layers is to grow Zn(S,Se) and (Zn,Mg)(S,Se)-based structures with appropriate composition such that the whole structure is pseudomorphic to the GaAs substrate. The Zn(S,Se) has been grown by the Purdue team and other groups with a sulfur fraction of approximately 7 percent, a value designed to lattice match ZnSe to the GaAs substrate [21]. The x-ray rocking curve diffraction peaks obtained from the Zn(S,Se) layers had full-widths-at-half-maximum of 20 to 65 arcseconds, which indicates a high degree of order in the crystal and a low misfit dislocation density. Transmission Electron Microscope (TEM) imaging further indicates that the dislocation densities are below $10^5/cm^2$. Fig. 1-2 shows a laser structure grown by the Purdue and Brown team is shown [16]. The Zn(S,Se)-based structures have ZnSe/(Zn,Cd)Se multiple quantum wells sandwiched within a Zn(S,Se) p-n homojunction. Zn(S,Se) with a S mole fraction of 7 to 8% is lattice-matched to the GaAs substrate such that the misfit dislocations are minimized. The optical confinement is due to the waveguiding resulting from the refractive index difference between MQW region and the adjacent Zn(S,Se) alloy. All materials were grown by molecular beam epitaxy. The devices operated as strong blue light emitting

diodes (LED) having output powers in excess of 100 μW and with external quantum efficiencies approaching 0.1% [16].

Using (Zn,Mg)(S,Se) lattice-matched to GaAs is another approach to avoid the lattice-mismatch between ZnSe and the GaAs substrate. Beside reducing misfit dislocations, (Zn,Mg)(S,Se) can also increase the bandgap energy so that it further improves the electronic confinement in ZnSe quantum wells. The (Zn,Mg)(S,Se) structure also opens the way to a separate confinement heterostructure with improved optical confinement properties. Fig. 1-3 is a schematic diagram of a ZnSe/(Zn,Mg)(S,Se) blue laser diode structure grown by the Sony group [22]. The epitaxial layers for the laser diode were grown by molecular beam epitaxy (MBE) at a substrate temperature of 240°C. The epitaxial layers were a p-type ZnSe cap layer(150 nm)/p-type (Zn,Mg)(S,Se) cladding layer (600 nm)/multiquantum-well layer/n-type (Zn,Mg)(S,Se) cladding layer (1 μm) on (100) n-type GaAs substrate. The MQW layer was composed of six quantum wells (ZnSe, 6nm) and five barrier layers ((Zn,Mg)(S,Se), 10 nm). (Zn,Mg)(S,Se) has 90% Zn and 18% S and is lattice-matched to the GaAs substrate. The difference in the bandgap energy between ZnSe and (Zn,Mg)(S,Se) is $\sim$ 0.2eV. Continuous wave operation of this device was achieved at 77K. Blue stimulated emission was observed at a wavelength of 477 nm and the threshold current density was 225 A/cm^2 [22].

Pseudomorphic II-VI epitaxial layers can significantly reduce the dislocation density of the films. However, the whole heterostructure is required to be lattice-matched to the GaAs substrate. Therefore, the design flexibility of the II-VI heterostructure is limited and an "alternative substrate" other than GaAs onto which II-VI compounds may be grown is desirable. From the bandgap versus lattice constant diagram, (In,Ga)P is an appropriate candidate as a substrate for II-VI compounds. By varying the In mole fraction, the lattice constant of the buffer layer can be varied to match that of any II-VI compound from ZnS (approximately lattice-matched to GaP) to ZnTe and CdSe (approximately matched by InP). By designing a proper (In,Ga)P structure lattice-matched to the II-VI layers, such as a superlattice, the strain-induced misfit dislocations are expected to be confined primarily near the (In,Ga)P/GaAs interface

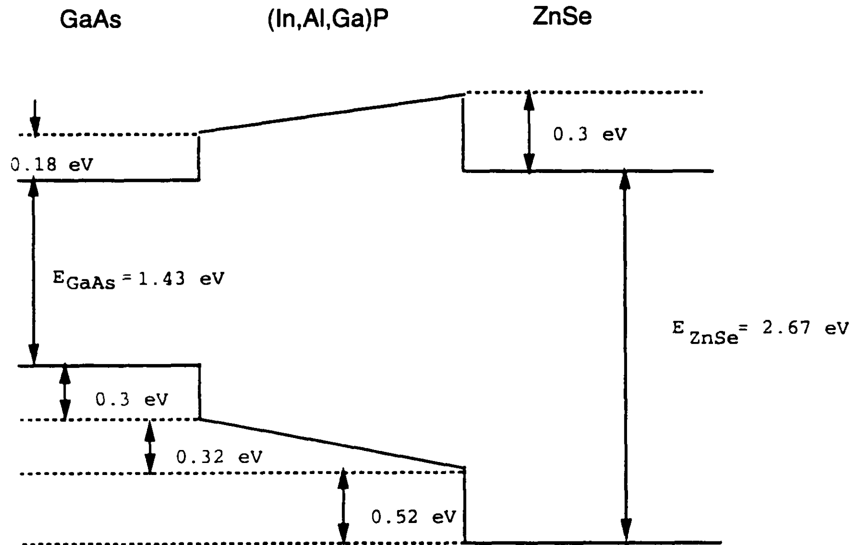

Figure 1-4: The energy band lineup of ZnSe/InGaP/GaAs heterostructure.

leaving the interface between ZnSe and (In,Ga)P free of dislocations.

(In,Ga)P can also reduce the barrier to hole injection presented by the heterojunction between p-GaAs and p-ZnSe. Gold is the most common contact material. But the Schottky barrier ($\sim$ 1 eV) of the gold contact obstructs the injection of holes from the connecting wire into the p-type ZnSe [23, 24]. However, the contact between gold and GaAs is ohmic, which suggests that (In,Ga)P can be used as an valence band offset reduction layer between ZnSe and (In,Ga)P. By grading (In,Ga,Al)P from (In,Ga)P to (In,Al)P, the valence band offset between thep-type ZnSe layer and the p-type III-V layer is reduced to 0.5 eV and therefore improves the hole transport from the III-V layer to the II-VI layer (Fig. 1-4).

In chapter 2, the gas source molecular beam epitaxial growth of (In,Ga)P and ZnSe epitaxial layers will be discussed. Then the growth conditions for (In,Ga)P and ZnSe will be given. Chapter 3 will give two possible models for estimation of critical thickness of lattice-mismatched heterostructures. In chapter 4, double crystal x-ray

diffraction measurements, and the structural properties of (In,Ga)P will be discussed. Chapter 5 will describe the photoluminescence of ZnSe on (In,Ga)P. Finally, the conclusions are summarized in chapter 6. Promising directions for future research will also be discussed.

Chapter 2

Epitaxial Growth

2.1 Gas Source Molecular Beam Epitaxy

The (In,Ga)P and ZnSe layers under investigation were grown in an unique molecular beam epitaxy system. Because Zn and Se are dopants for all III-V materials, ZnSe and III-V materials have to be grown in separate chambers to avoid any cross contamination. Our unique gas source molecular beam epitaxy (GSMBE) system consists of two independent growth reactors, one transfer chamber, one analytical chamber, one buffer chamber, and one introduction chamber. A schematic of the system is shown in Fig. 2-1.

Samples are first loaded into the introduction chamber which has the capacity of accepting 5 sample holders at a time. The introduction chamber can be pumped down to the 10^{-9} Torr range. The sample is then transferred into the transfer chamber using a robotic arm located at the center of the transfer chamber. The transfer chamber serves as a traffic center and wafer storage area for the whole system. The robotic arm is controlled by three stepper motors and can perform three dimensional movement. The arm can be extended and retracted, moved up and down, and also can be rotated around its central axis. The samples are first heated on a heating stage inside the transfer chamber at 200°C for 60 minutes prior to growth to evaporate the moisture and any acid residue from etching. The sample is then transferred into the III-V buffer chamber. Because of the incompatibility of the sample holder for the II-VI

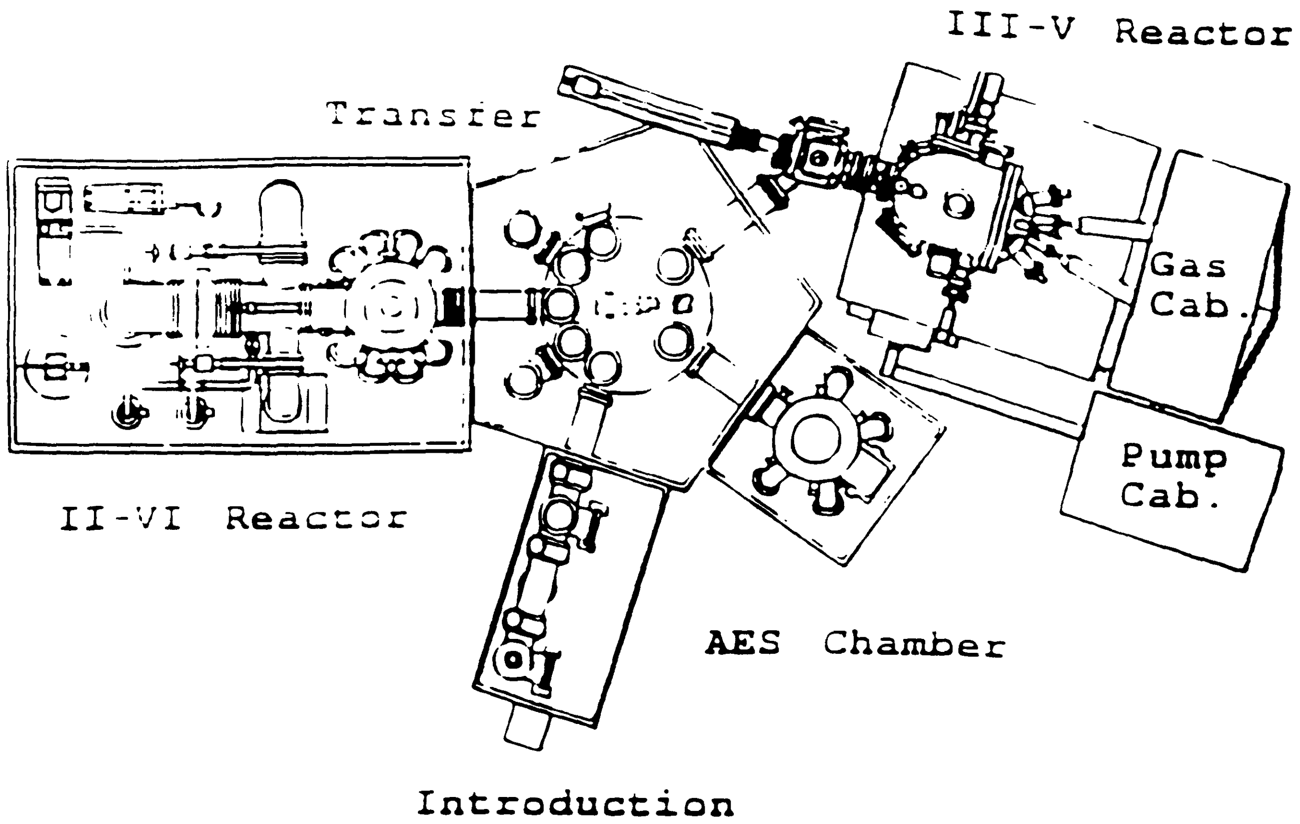

Figure 2-1: Schematic layout of the principal components of the II-VI and III-V gas source molecular beam epitaxy system.

reactor and III-V reactor, the II-VI holder is coupled to a custom-designed III-V holder using a five degrees of freedom manipulator and a wobble stick inside the buffer chamber. The base pressure of the transfer chamber and III-V buffer chamber is typically 1-2$\times 10^{-10}$ Torr. The ultrahigh vaccum in both chambers minimizes the contamination introduced during the transfer process from the III-V chamber to the II-VI chamber keeping the interface between III-V layers and II-VI layers free of contaminants. The formation of the interface between III-V layers and II-VI layers is critical to the growth of high quality heterostructures.

The III-V growth chamber is a Riber CBE 32P reactor (Fig. 2-2). The principal operative systems in the MBE reactor and their functions are listed in Table 2.1. The whole chamber is pumped by a Balzers 2200 liter per second turbomolecular drag pump backed by a mechanic pump, and a cryogenic pump. The MBE process environment is ultrahigh vacuum, i.e. $\sim 10^{-10}$ Torr. During the growth, because the effusion cells and the substrate holder are maintained at high temperatures, and a large amount of H_2 is introduced into the chamber by the gas sources during growth, the chamber pressure is around 10^{-5}Torr. A liquid nitrogen cryopanel is used to cool the chamber temperature to 77K during the growth period in order to reduce the chamber pressure and thus reduce the background impurities. Impurities not emanating from the beam source material or the crucible will have to suffer at least one collision with a liquid nitrogen cooled surface prior to reaching the growth environment. The residual gas analyzer is used to analyze the gaseous species in the chamber. A reflection high energy electron diffraction setup is used to monitor *in situ* the surface of the epitaxial layer during the growth (to be discussed in detail later).

The substrate temperature measurement is achieved using a thermocouple that is carefully positioned in a black-body enclosure situated behind the sample holder. An infrared pyrometer is used for direct measurement of the substrate temperature by viewing the substrate through a viewport. An "AuGe eutectic" or an InSb substrate is used to calibrate the emissivity of the pyrometer. AuGe undergoes an eutectic phase transition at 356°C, while InSb undergoes a solid-to-liquid phase transition at

Function	Hardware	Objective
In, Ga, Al, Si, Be molecular beam sources As, P beam sources	Knudsen cells Gas cracking cells	To provide stable, high purity, atomic or molecular beams impinging onto the substrate surface
Molecular beam interruptors	Fast action shutters	To complete close or open the cells within 0.1 second
Growth-time surface monitor	Reflection High Energy Electron Diffraction Diffraction (RHEED)	To monitor *in situ* the surface structure of the substrate and epitaxial films
Flux monitor	Ion gauge	To calibrate the beam flux
Impurity monitor	Quadruple mass spectrometer	To monitor background impurities

Table 2.1: Principle components and their functions in a MBE system

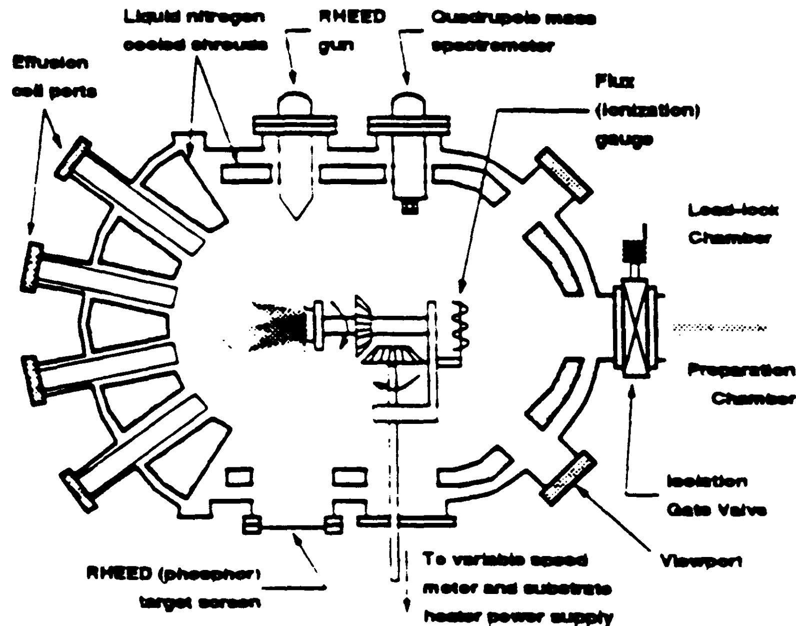

Figure 2-2: Schematic diagram of the GSMBE system utilized for the growth of p- and n-type (In,Ga)P and other III-V compound semiconductors [26].

525°C. In order to avoid thickness and composition nonuniformity due to overlapping cosinusoidal distributions from each Knudsen source, the substrate is rotated in a plane orthogonal to the direction of the incident beams. In our experiments, the rotation speed is usually kept at $\sim$ 3 rpm. The thickness nonuniformity reported by the manufacturer is within $\pm 1\%$ across a 3 inch wafer.

The III-V growth chamber has 5 solid source Knudsen effusion cells containing In, Ga, Al, Be, and Si. Among them, Be is the p-type dopant and Si is the n-type dopant for (In,Ga)P. The molecular beam flux and atom arrival rates at the substrate surface are calculated from the relevant vapor pressure data and the system geometry. Under the conditions of ultralow pressure, the mean free path of a molecule is larger than the distance from the effusion cell to the substrate surface. There are no collisions between source molecules and gas molecules. The process can be simplified as line-of sight evaporation into a perfect vacuum [25]. The flux in such a system is

$$F_D = \frac{P_D}{\sqrt{2\pi M_D k T_D}} \tag{2.1}$$

where P_D is the equilibrium vapor pressure of source D, M_D is the mass of species D, T_D is the absolute temperature of the effusion cell, and k is the Boltzmann constant. The vapor pressure P_D is an exponential function of temperature:

$$P_D = P_{0,D} e^{-E_{A,D}/kT_D} \tag{2.2}$$

where $E_{A,D}$ is the activation energy and $P_{0,D}$ is a constant independent of temperature. By combining Eq. 2.1 and Eq. 2.2,

$$F_D = \frac{P_{0,D} e^{-E_{A,D}/kT_D}}{\sqrt{2\pi M_D k T_D}}. \tag{2.3}$$

is obtained.

A series of experiments have been performed to find the relationship between flux and cell temperature. Fig. 2-3 shows the experimental Ga flux versus temperature, in addition to a theoretical fit using Eq. 2.3. The fluxes were measured by a flux ion

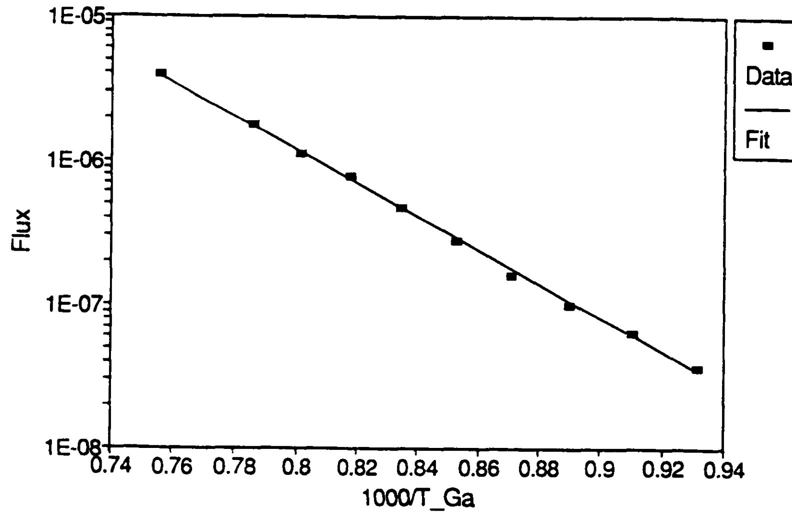

Figure 2-3: The experimental Ga flux versus temperature diagram and its theoretical fit using Eq.2.3.

gauge. The exponential approximation model is found to be very accurate in determining the behavior of the Knudsen effusion cells. In most III-V epitaxial growth, Group III-controlled growth is used, which means that there are always excess Group V species present on the epitaxial surface. By measuring the In, Ga, or any other Group III species' flux, the layer composition can be accurately controlled.

For a fixed effusion cell temperature, it was observed experimentally that the flux decreases in the initial 2 minutes following opening of the shutter (Fig. 2-4). This is believed to be thermal losses due to black body radiation. When the shutter is closed, the cell is treated as a isolated black body which is at equilibrium in temperature. After the shutter is opened, the cell is no longer an ideal black body. The cell now faces a much cooler surrounding environment. The radiated heat loss will cause the temperature on the surface of the cell to drop and the flux will also drop by as much as 10% in the first 2 minutes. The flux transient poses a serious problem for the growth of quantum well nanostructures whose layer thickness is usually 10-1000 Å. The initial flux transition can severely affect the composition control within the quantum well, and therefore degrade the potential modulation in the well. Much effort has been devoted to the elimination of the flux transition. By carefully modulating

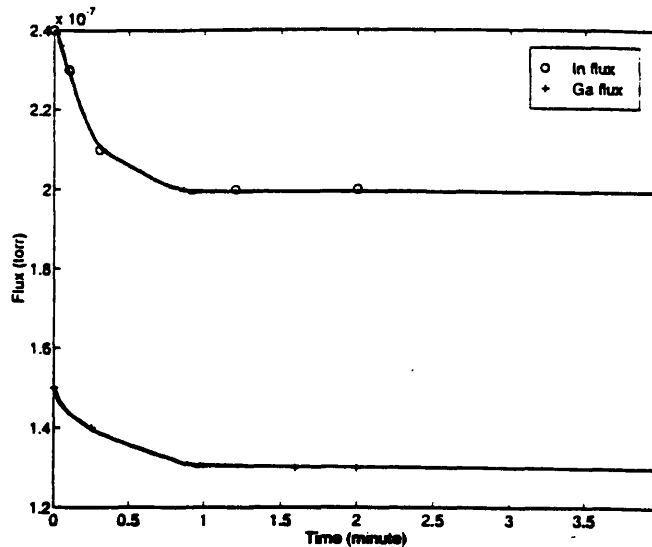

Figure 2-4: In and Ga flux transition during the initial 5 minutes after the substrate shutter is opened. The lines are drawn to guide the eye.

the temperature of the cell, Vleck et. al. [26] has reported a flux transition of only 1%. A secondary problem which has also been observed is a consistent flux drop over a long period of time (Fig. 2-5). This is due to the depletion of the source material inside the cell. Therefore, it is necessary to routinely measure the flux in order to compensate for any flux decrease.

There are two kinds of macroscopic defects that are believed to be caused by imperfections in the behavior of the Knudsen effusion cells. The defects are: (i) irregularly shaped hilllocks or pits (Fig. 2-6) which are created by dissolution and regrowth of III-V layers following impact of a Ga droplet on the surface [27], and (ii) oval defects (Fig. 2-7) which are oriented along a given crystallographic direction and may be associated with a localized surface contaminant. Pits are believed to be associated with Ga droplet "spitting" from the Ga crucible [28]. The spitting from the Ga oven is related to the build up of Ga droplets around the orifice of the crucible. It has been shown that these defects are eliminated by a long bakeout of the growth chamber. This suggests that the spitting is probably related to the presence of an impurity layer on the surface of the Ga source due to the reaction between the Ga and the residual gases such as water vapor in the vacuum chamber.

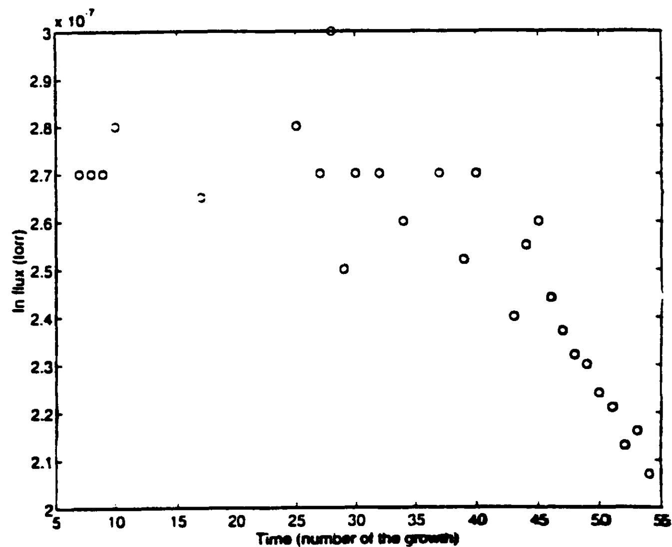

Figure 2-5: The In flux measured by a flux ion gauge over a period of six months.

Oval defects are oriented in the $[1\bar{1}0]$ direction on a (001)-oriented substrate and vary in length from 1 to 10 μm, and in density from 10^3 to $10^5/\text{cm}^2$ depending on growth and system conditions. It is reported that these defects are microtwins that originate at local imperfections [29]. Substrate surface contamination by carbon has been cited as one of the possible causes [29]. Ga and In fluxes are also believed to play a major role in the defect formation [30]. Oval defects have not been observed in the (In,Ga)P grown on a GaAs substrate in this study. However, these defects are clearly visible for InP and (In,Ga)(As,P) films grown on InP substrates using the same machine during the same period. The observation suggests that the In and Ga fluxes are not the deciding factors in the formation of oval defects since both kinds of films were grown using the same In and Ga cells. A more detailed study is needed to further clarify this phenomenon.

Our system uses AsH_3 and PH_3 as group V sources instead of the regular solid group V source. The undiluted high-purity gases are thermally decomposed or "cracked" into dimers of As_2 and P_2 at 900°C in a gas cracker. The cracking efficiency is about 90% to 100%. The major products of the dissociation are the dimers, some tetramers, H_2, and residual hydrides. The fluxes of AsH_3 and PH_3 are controlled by two separate mass flow controllers which can regulate the gas with 0.5% accuracy.

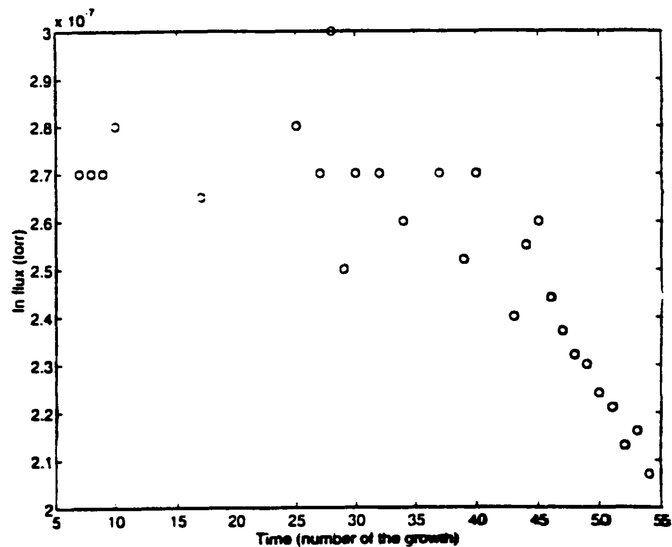

Figure 2-5: The In flux measured by a flux ion gauge over a period of six months.

Oval defects are oriented in the $[1\bar{1}0]$ direction on a (001)-oriented substrate and vary in length from 1 to 10 μm, and in density from 10^3 to $10^5/cm^2$ depending on growth and system conditions. It is reported that these defects are microtwins that originate at local imperfections [29]. Substrate surface contamination by carbon has been cited as one of the possible causes [29]. Ga and In fluxes are also believed to play a major role in the defect formation [30]. Oval defects have not been observed in the (In,Ga)P grown on a GaAs substrate in this study. However, these defects are clearly visible for InP and (In,Ga)(As,P) films grown on InP substrates using the same machine during the same period. The observation suggests that the In and Ga fluxes are not the deciding factors in the formation of oval defects since both kinds of films were grown using the same In and Ga cells. A more detailed study is needed to further clarify this phenomenon.

Our system uses AsH_3 and PH_3 as group V sources instead of the regular solid group V source. The undiluted high-purity gases are thermally decomposed or "cracked" into dimers of As_2 and P_2 at 900°C in a gas cracker. The cracking efficiency is about 90% to 100%. The major products of the dissociation are the dimers, some tetramers, H_2, and residual hydrides. The fluxes of AsH_3 and PH_3 are controlled by two separate mass flow controllers which can regulate the gas with 0.5% accuracy.

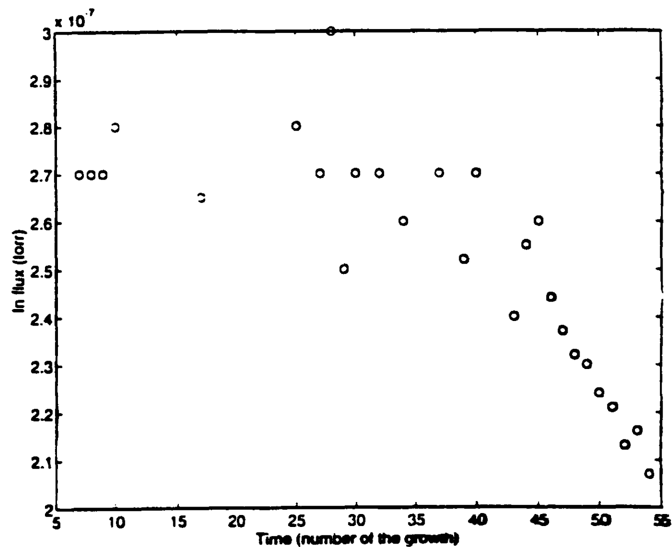

Figure 2-5: The In flux measured by a flux ion gauge over a period of six months.

Oval defects are oriented in the $[1\bar{1}0]$ direction on a (001)-oriented substrate and vary in length from 1 to 10 μm, and in density from 10^3 to $10^5/\text{cm}^2$ depending on growth and system conditions. It is reported that these defects are microtwins that originate at local imperfections [29]. Substrate surface contamination by carbon has been cited as one of the possible causes [29]. Ga and In fluxes are also believed to play a major role in the defect formation [30]. Oval defects have not been observed in the (In,Ga)P grown on a GaAs substrate in this study. However, these defects are clearly visible for InP and (In,Ga)(As,P) films grown on InP substrates using the same machine during the same period. The observation suggests that the In and Ga fluxes are not the deciding factors in the formation of oval defects since both kinds of films were grown using the same In and Ga cells. A more detailed study is needed to further clarify this phenomenon.

Our system uses AsH_3 and PH_3 as group V sources instead of the regular solid group V source. The undiluted high-purity gases are thermally decomposed or "cracked" into dimers of As_2 and P_2 at 900°C in a gas cracker. The cracking efficiency is about 90% to 100%. The major products of the dissociation are the dimers, some tetramers, H_2, and residual hydrides. The fluxes of AsH_3 and PH_3 are controlled by two separate mass flow controllers which can regulate the gas with 0.5% accuracy.

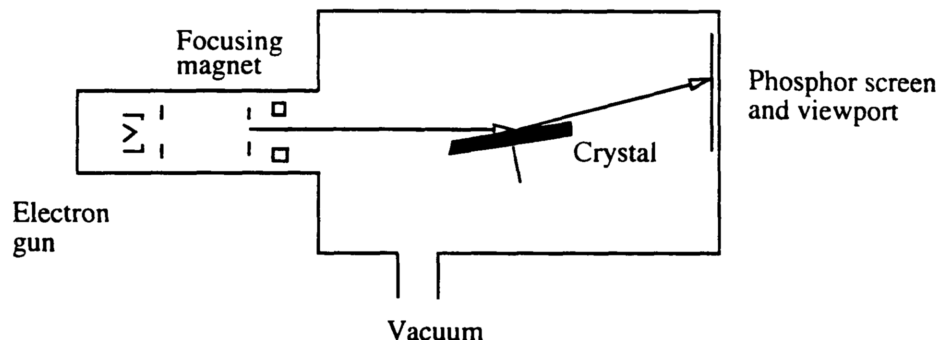

Figure 2-8: A schematic diagram of a typical RHEED setup contained in a molecular beam epitaxy system.

streaks will be quite short [32, 33]. Long streaks are reported to indicate an angular uncertainty or energy uncertainty in the beam source or they originate from surface dislocation planes during growth [33].

Reflection high energy electron diffraction is used in MBE to monitor the oxide desorption. Before the oxide on the GaAs or InP substrate is desorbed prior to growth, a RHEED pattern is not observed because the oxide is amorphous and has no periodic structure. When the oxide begins to desorb, the underlying periodic crystal structure diffracts the incoming electron beam and forms a periodic intensity pattern on the RHEED screen. Group V overpressure is usually applied during the desorption of the oxide to compensate for Group V desorption and maintain a Group V-rich surface. At the temperature of around 580°C where the oxide begins to desorb, the streaks of the GaAs diffraction pattern will slowly appear. The RHEED pattern at 580°C is shown in Fig. 2-10. The lines along the $[1\bar{1}0]$ are weak in intensity with a diffusive background intensity. The streaks will gradually become more and more intense as the substrate temperature increases and the oxide evaporates. The RHEED pattern at 620°C is shown in Fig. 2-11. The (2×4) RHEED pattern is clearly observed along $[\bar{1}\bar{1}0]$ and $[1\bar{1}0]$ orientations. The line aspect of the RHEED reconstruction pattern is

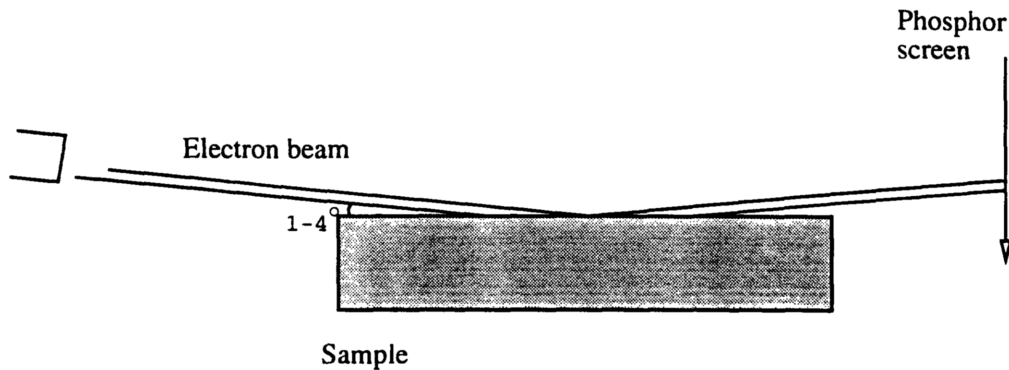

Figure 2-9: Electron beam penetrates the sample at a very small angle. Although the beam travels a long distance ($\sim$ several mm) inside the sample, the effective penetration depth is very small ($\sim$ 10-20 $\AA$).

a reflection of the quality of the substrate surface crystallography. The presence of diffusive dots or arrow heads is characteristic of a three dimensional surface due to bad substrate preparation. A well prepared substrate will show sharp 2×4 streaks.

The RHEED reconstruction pattern can also be used to monitor the growth mode. For an epitaxial film grown on a lattice-matched substrate by MBE, the growth proceeds in the Frank-van der Merwe mode [34]. In this growth mode, epitaxial growth takes place in a two-dimensional manner, with the completion of one monolayer before the next monolayer begins to grow (Fig. 2-12). The RHEED reconstruction therefore shows a streaked pattern. However, if an epitaxial layer is grown on a lattice-mismatched substrate, misfit dislocations will be generated to relieve the strain if the film thickness is larger than the critical thickness. These dislocations will serve as sites for the nucleation of clusters and three dimensional (3D) growth will occur. In the 3-D growth mode, instead of layer-by layer formation, islands will be formed. RHEED reconstruction will show a circular spot pattern instead of a streaky pattern. The transition from 2-D growth to 3-D growth has been observed in the growth experiments. A $In_{0.5}Ga_{0.5}As$ film is grown on a lattice-mismatched GaAs substrate.

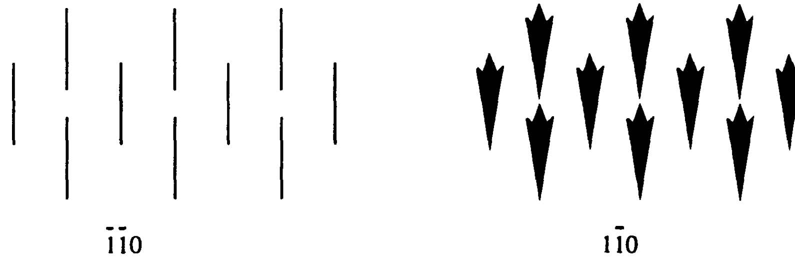

Figure 2-10: The RHEED reconstruction pattern of the GaAs substrate observed at 580°C.

During the initial 6 seconds, the RHEED reconstruction maintains a streaky pattern which suggests a layer-by-layer growth mode. However, after 6 seconds, the streaky RHEED pattern suddenly becomes spotty and exhibits a circular spot pattern, which indicates a 3D growth mode. From the observation of this transition and the knowledge of the growth rate, a zero-order estimation of the threshold thickness at which the growth mode changes from 2-D to 3-D growth can be obtained.

In the layer-by-layer growth mode, the intensity of the streaky pattern will vary during the formation of a perfect planar layer. The RHEED intensity oscillation is used to monitor *in situ* the formation of each layer. In addition, the RHEED intensity oscillation is often used to measure *in situ* the growth rate of the film. One period of a RHEED intensity oscillation indicates the formation of one monolayer of GaAs or InP. For a typical (100)-oriented III-V surface with zincblende structure, one unit cell consists of two monolayers of GaAs or InP. The growth rate v of the film is determined by finding the period T of the RHEED oscillation and then use

$$v = \frac{a}{2T} \tag{2.5}$$

where a is the lattice constant of the epitaxial layer. An example is shown in Fig. 2-13.

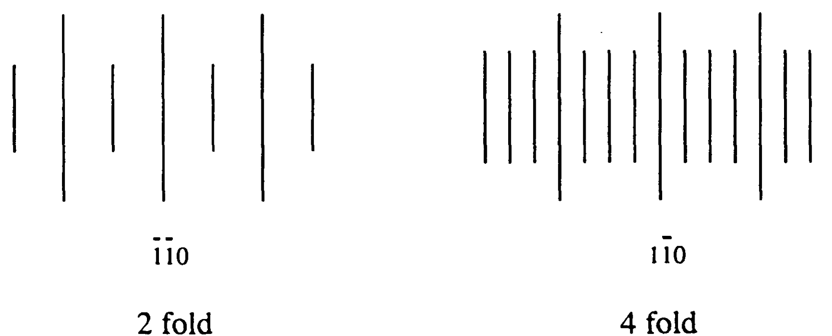

Figure 2-11: The RHEED reconstruction pattern of the GaAs substrate observed at 620°C.

The period of the RHEED intensity oscillation is 2.91 seconds. By using Eq. 2.5, the growth rate of this film is 0.97 Å/sec. Furthermore, all III-V compounds are grown under a Group V-rich condition. The growth rate is determined by the Group III arrival rate. Therefore, if the In and Ga arrival rates are known, the composition of the ternary compound is obtained. In the experiment, the Ga arrival rate is first measured by the GaAs RHEED intensity oscillation. The indium plus gallium arrival rate is measured by the (In,Ga)P RHEED intensity oscillation. The Ga composition in the (In,Ga)P is then determined by

$$x = \frac{v_{Ga}}{v_{InGaP}}. \tag{2.6}$$

One problem associated with this method has been alluded to previously. The problem is associated with the flux transition present after the shutter is open. The flux does not stabilize until 4 or 5 minutes after the shutter is open. However, the typical RHEED intensity oscillation only persists for a few minutes. Therefore it will not be accurate if the RHEED intensity oscillation obtained immediately after the shutter is open is used. Before the shutter is open, the surface is flat and the RHEED intensity is high. Once the shuttle is open, the surface starts to roughen and

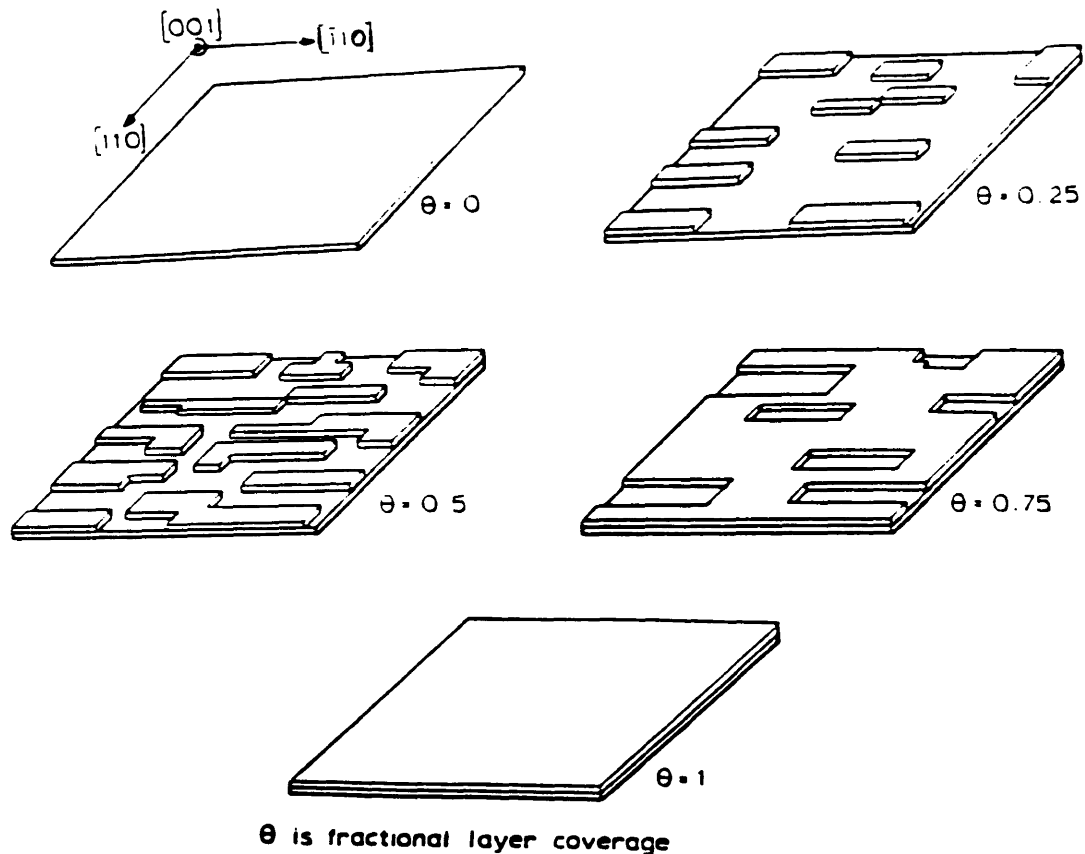

Figure 2-12: In the layer-by-layer growth mode, epitaxial growth proceeds in a two-dimensional manner, with the completion of one monolayer before the next monolayer begins to grow.

the RHEED intensity decreases. After one monolayer is formed, the surface becomes planar again. This forms one cycle of the RHEED intensity oscillation. However, after a number of layers have been formed, the surface will no longer be perfectly planar due to incomplete layer coverage, and the RHEED intensity oscillation will be dampened out and disappear. Fig. 2-14 is a typical (In,Ga)P RHEED intensity oscillation obtained during the experiment. By using Eq. 2.5, the relationship between the growth rate and time is found. As seen in Fig 2-15, the measured growth rate is decreasing with time as determined by the changing period of intensity oscillation. Therefore, this data can not be used evaluate the real growth rate and Ga mole fraction.

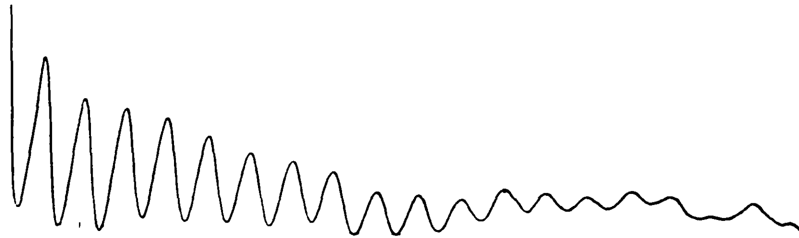

Figure 2-13: A typical GaAs RHEED intensity oscillation measurement with a growth rate of 0.39 μm/hour.

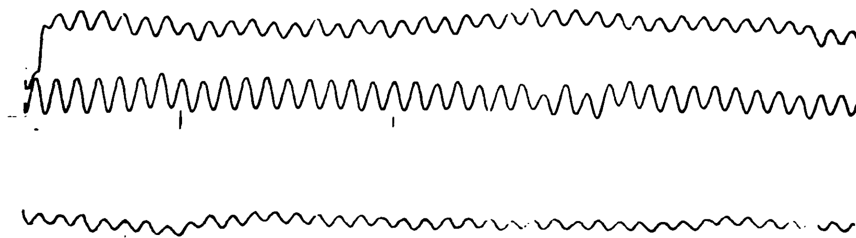

Figure 2-14: A typical (In,Ga)P RHEED intensity oscillation measurement with a growth rate of 0.8 μm/hour

Alternatively, instead of measuring the RHEED intensity oscillation at the start of the growth, a more precise method is to measure the RHEED intensity oscillation during the growth when the shutter has been open for a long time. To perform the measurement during the growth, the Group V shutter is closed for a very short period of time ($\sim$ 1 second), then the shutter is reopened. The shutter close time is chosen such that it is short enough to avoid the formation of a Group III rich surface which destroys the layer-by-layer growth mode. After the shutter is reopened, 5 to 6 periods of RHEED intensity oscillations are obtained (Fig. 2-16). From these

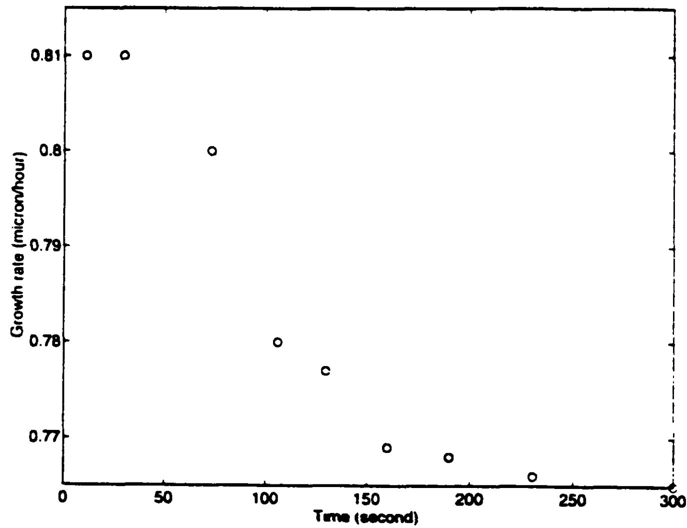

Figure 2-15: The growth rate measured from (In,Ga)P RHEED intensity oscillations decreases over time from the start of the growth.

RHEED intensity oscillations, the steady state Group III arrival rate is determined. For (In,Ga)P epitaxial growth, up to 6 minutes of RHEED intensity oscillations is obtained (Fig. 2-17). The duration of the RHEED intensity oscillation is sufficient such that the steady state growth rate of (In,Ga)P is measured. From these two pieces of data, the composition of the (In,Ga)P buffer layer is accurately determined.

2.3 Growth Procedure

In this section, the (In,Ga)P and ZnSe growth procedures and growth conditions will be discussed.

2.3.1 Substrate Preparation

The GaAs substrate is first degreased by a standard degreasing procedure. The detailed degreasing procedure is listed in Table 2.2. The degreased substrate is then etched in a freshly prepared mixture of H_2SO_4:H_2O_2:H_2O for 90 seconds, the proportions of the etch are 5:1:1. The etch mixture is then progressively diluted with deionized (DI) water leaving the oxidized substrate submerged in pure DI water. The

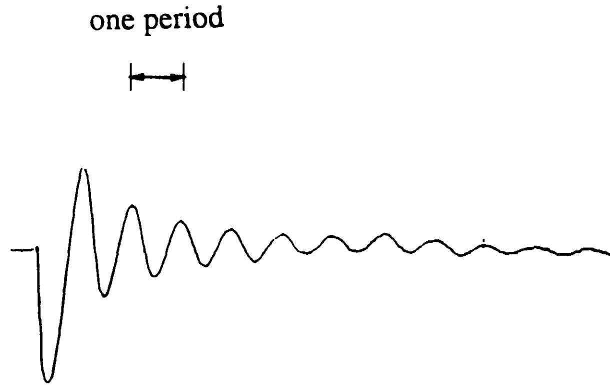

Figure 2-16: GaAs RHEED intensity oscillation obtained by closing the AsH_3 shutter for a very short time (~ 1 second) during the growth followed by resuming the GaAs growth.

Time	Method
10 munites	Boiled in trichrolethine
10 minutes	Boiled in trichrolethine
15 minutes	immersed in Aceton in a ultrasonic cleaner
15 minutes	immersed in Methanol in a ultrasonic cleaner

Table 2.2: Degreasing procedure for GaAs substrates

substrate is blown dry with filtered nitrogen gas.

The degreased, etched sample is then mounted onto a molybdenum sample holder using high purity indium solder. Indium melts at 156°C, therefore, the molybdenum sample holder is heated to 156° on a hot plate in order to melt the indium and allow the In to wet the Mo surface. However, in some experiments, following the growth of the (In,Ga)P buffer layer, the sample is dismounted from the sample holder and transferred to a II-VI-dedicated sample holder for the subsequent growth of ZnSe. Ga is liquid at room temperature such that it is not necessary to heat the sample holder to remove the substrate. In order to avoid oxidation and adsorption of other contaminants from the atmosphere, Ga is used to mount the substrate. An InSb

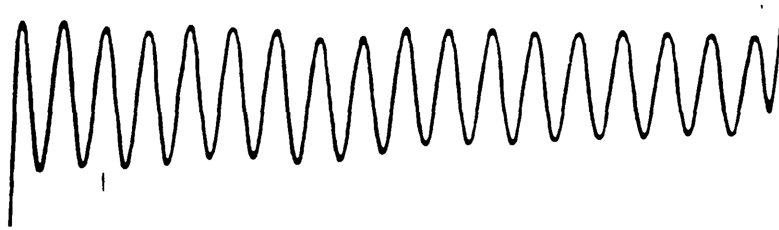

Figure 2-17: (In,Ga)P RHEED intensity oscillation obtained at the beginning of an (In,Ga)P growth; the oscillations last for over 5 minutes.

substrate is also mounted on the GaAs substrate to calibrate the growth temperature since InSb melts at 525°C. The GaAs substrate and sample holder are then placed in the buffer chamber prior to insertion into the growth reactor.

2.3.2 (In,Ga)P Growth

To initiate growth, the GaAs substrate is transferred into the growth chamber from the buffer chamber. With the substrate at the transfer position, the substrate temperature is raised to 200°C, while the In, Ga, and AsH_3/PH_3 cracker temperatures are set at the desired temperature. After the cell temperatures are equilibrated, the In and Ga fluxes are measured by using the flux ion gauge. The In and Ga cell temperatures are then ramped down to 725°C and 825°C, respectively to conserve the source material during the oxide desorption period. With an As flux impinging onto the substrate surface, the substrate temperature is gradually increased to 630°C. During this period, the InSb solid-to-liquid phase transition at 525°C is observed. The observation of the phase transition is used to calibrate the substrate temperature. The substrate oxide starts to desorb at 575°C and a (2×4) RHEED reconstruction pattern is eventually observed. When the substrate temperature reaches 630°C, the oxide is

completely desorbed and a clear (2×4) RHEED pattern is observed. The substrate temperature is kept at 630°C for 10 minutes to desorb any residual acid and other contaminants. After the oxide desorption, the substrate temperature is ramped down to 600°C and the growth of a 0.5 μm GaAs buffer layer occurs. The chamber pressure during the growth is 1.4×10^{-5} Torr. The growth rate is 0.8 μm/hour. The Group V to Group III ratio is approximately 10:1 as determined from the RHEED intensity oscillation and the flux measurement. The atomic Ga arrival rate is determined by measuring the GaAs RHEED intensity oscillation.

The substrate temperature is then decreased to 450°C as determined by a thermal couple calibrated by the InSb melting temperature. The (In,Ga)P growth proceeds by switching the AsH_3 to PH_3 and opening the In and Ga source shutters. The (In,Ga)P is grown for 5 minutes and the (In,Ga)P RHEED intensity oscillation is measured. The In arrival rate and the (In,Ga)P composition are determined from the RHEED intensity oscillation measurement. After the RHEED intensity oscillation measurement, the (In,Ga)P buffer layer is grown for four hours. The chamber pressure during the growth is 1.2×10^{-5}Torr. The growth rate is typically 0.8 μm/hour. The RHEED reconstruction pattern during the growth is (2×1). After the growth is completed, the (In,Ga)P is coated *in situ* with amorphous arsenic to passivate the surface for the *ex situ* transfer to the II-VI GSMBE reactor.

The passivating layer of amorphous arsenic is then desorbed in the II-VI growth chamber at approximately 270 °C until recovery of the (2×1) reconstruction RHEED pattern is observed which is characteristic of the (In,Ga)P surface.

2.4 ZnSe Growth Procedure

The ZnSe is grown with elemental Zn and gaseous H_2Se at growth temperatures ranging from 240 °C to 330 °C, although a majority of the films are grown at 270°C. The substrate temperature is calibrated by observing the eutectic phase transition (356°C) of 500Å of Au that was deposited onto Ge, and is continuously monitored using an optical pyrometer. The H_2Se gas flow is varied from 0.8 to 1.5 sccm by

a mass flow controller. The H_2Se was thermally decomposed in an EPI gas cracker at 1000°C. The zinc flux, as measured by a water-cooled crystal oscillator placed in the substrate position, corresponded to a zinc deposition rate ranging from 0.5 to 0.8 Å/s. Under these conditions, the Se:Zn flux ratio ranged from 1.3:1 to 0.6:1. The resulting chamber pressure is approximately 2×10^{-5} Torr during growth. During the epitaxial growth process, the surface stoichiometry was monitored by observing the surface reconstruction using reflection high energy electron diffraction. The ZnSe is grown at rates of 0.3 to 0.5 μm/hour to layer thicknesses of 1.5 to 2 μm.

Chapter 3

Critical Thickness

In order to grow high quality ZnSe on lattice-matched (In,Ga)P buffer layers, it is critical that (In,Ga)P buffer layers on GaAs substrates are relaxed and not elastically strained. For lattice-mismatched epitaxial layers, it is well known that below a certain critical thickness, the misfit between the epitaxial layer and substrate will be accommodated by uniform elastic strain and the in-plane lattice constant $a_{||}$ of the epitaxial layer will be equal to the lattice constant of the substrate [34]. If the thickness of (In,Ga)P is below the critical thickness, the in-plane lattice constant will be lattice-matched or the same as $a_{||}$ of the GaAs substrate, thus the ZnSe will still be lattice-mismatched to the (In,Ga)P buffer layer. Misfit dislocations will be formed in the ZnSe layer in order to relieve the homogeneous strain energy. These dislocations will severely degrade the optical and electrical properties of II-VI devices. It is therefore important that the thickness of the (In,Ga)P buffer layer is larger than the critical thickness. In this chapter, two theories that evaluate the critical layer thickness, h_c, will be introduced.

3.1 Force-Balancing Model

J. W. Matthews and A. E. Blakeslee first proposed a lattice-matching model by balancing the force, F_ϵ, exerted by the misfit strain on a grown-in threading dislocation and the tension, F_l, in the dislocation line [35]. If one considers an epitaxial layer A

on a lattice-mismatched substrate B (Fig. 3-1) assuming isotropic elastic constants, then

$$F_\epsilon = \frac{2G(1+\nu)}{(1-\nu)} bh\epsilon \cos\alpha. \tag{3.1}$$

G is the shear modulus, b is the magnitude of the Burgers vector of the dislocation($\frac{a}{\sqrt{2}}$), ϵ is the misfit strain $\epsilon = \frac{a_{epi}-a_{sub}}{a_{sub}}$, ν is the Poisson ratio and α is the angle between the slip direction and that direction in the film plane which is perpendicular to the line of intersection of the slip plane and the interface. h is the thickness of the film. The tension in the dislocation line can be approximately described by

$$F_l = \frac{Gb^2}{4\pi(1-\nu)}(1-\nu\cos^2\theta)\left[\ln\left(\frac{b}{a}\right)+1\right], \tag{3.2}$$

where θ is the angle between the dislocation line and its Burgers vector. If F_ϵ is less than F_l, then the interface between layer and substrate will be coherent and the misfit will be accommodated by the strain. However, if F_ϵ is larger than F_l, dislocations will move and the coherence of the interface will be destroyed. Therefore, the critical thickness can be defined as the h that satisfies $F_\epsilon = F_l$. The solution can be obtained from

$$h_c = \frac{b}{8\pi\epsilon}\frac{1-\nu\cos^2\theta}{(1+\nu)\cos\alpha}\left[\ln\left(\frac{h_c}{b}\right)+1\right]. \tag{3.3}$$

Poisson ratio ν is defined as

$$\nu = \frac{C_{12}}{C_{11}+C_{12}}. \tag{3.4}$$

For $In_{0.52}Ga_{0.48}P$, and using Vegard's law, C_{11} is equal to 1.2092×10^{12}dyn/cm^2, and C_{12} is equal to 0.59952×10^{12}dyn/cm^2. The Poisson ratio ν is 0.33. θ is 60° for most III-V semiconductors. α is 60°. The misfit strain between the stress-free epitaxial layer and the substrate is 0.25%. Solving Eq. 3.3 numerically, h_c is found to be 47 nm. In contrast to the theory, for a 1 μm $In_{0.52}Ga_{0.48}P$ epitaxial layer, the (511) x-ray diffraction rocking curve measurements show that the in-plane lattice constant of the (In,Ga)P is equal to the bulk lattice constant of the GaAs substrate. No dislocations are observed by transmission electron microscope (Fig. 3-2) [36]. These observations indicate that the films are still pseudomorphic to the GaAs substrate, and there-

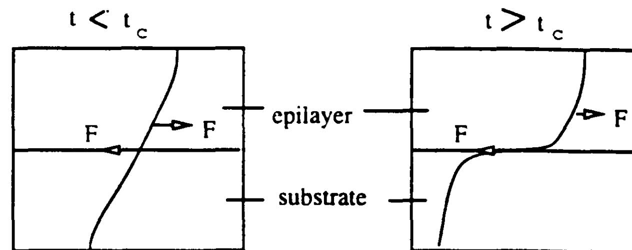

Figure 3-1: Forces applied on an epitaxial layer A on a lattice-mismatched substrate B.

fore the force-balancing model provides a considerably smaller h_c than that observed experimentally. Therefore, the force-balancing model may not be appropriate for evaluation of the critical thickness for (In,Ga)P having a small lattice-mismatch to GaAs.

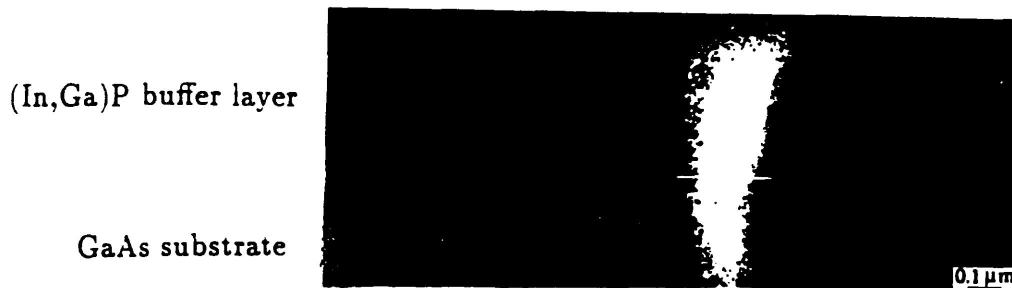

Figure 3-2: Cross-sectional high resolution transmission electron micrograph of an (In,Ga)P buffer layer on a GaAs substrate [36].

3.2 Energy-Balancing Model

In the force-balancing model [35], mechanical equilibrium of a grown-in threading dislocation determines the onset of interfacial misfit dislocation. In the energy-balancing model [37], the growing film is assumed to be initially free of threading dislocations. Interfacial misfit dislocations will be generated only when the areal strain energy density exceeds the self-energy of an isolated screw or edge dislocation [37]. The areal strain energy density associated with a film of thickness h is given by

$$\epsilon_H = 2G\left(\frac{1+\nu}{1-\nu}\right)\left(\cos^2\theta + \frac{\sin^2\theta}{1-\nu}\right)hf^2, \tag{3.5}$$

where f is the misfit strain, θ is the angle between the dislocation line and its Burgers vector (60° for almost all III-V semiconductors).

The energy density of screw, edge, and half-loop dislocations has been calculated by Nabarro [38]. Among those types of dislocations, the screw dislocation has the minimum energy density. It is a factor of $1/(1-\nu)$ smaller than the edge dislocation energy density. The areal energy density associated with an isolated screw dislocation at a distance h from a free surface is approximately

$$\epsilon_D \simeq \left(\frac{Gb^2}{8\pi\sqrt{2}a(x)}\right) ln\left(\frac{h}{b}\right), \tag{3.6}$$

where a(x) is the bulk lattice constant of the film and h denotes the film thickness. Similar to the force-balancing model, the critical thickness h_c is defined such that ϵ_H is equal to ϵ_D. If ϵ_H is less than ϵ_D, a coherent interface exists and the epitaxial layer is elastically strained, i.e. $a_{||}$ will be equal to the substrate lattice constant. h_c can be solved using

$$h_c = \left(\frac{1-\nu}{1+\nu}\right)\left[\cos^2\theta + \frac{\sin^2\theta}{1-\nu}\left(\frac{1}{16\pi\sqrt{2}}\right)\times\left(\frac{b^2}{a}\right)\right]\left[\left(\frac{1}{f^2}\right)\times\ln\left(\frac{h_c}{b}\right)\right]. \tag{3.7}$$

Using Eq. 3.7 to calculate the critical thickness for $In_{0.52}Ga_{0.48}P$ on GaAs, the critical thickness is 3.4 μm which is significantly larger than the critical thickness calculated

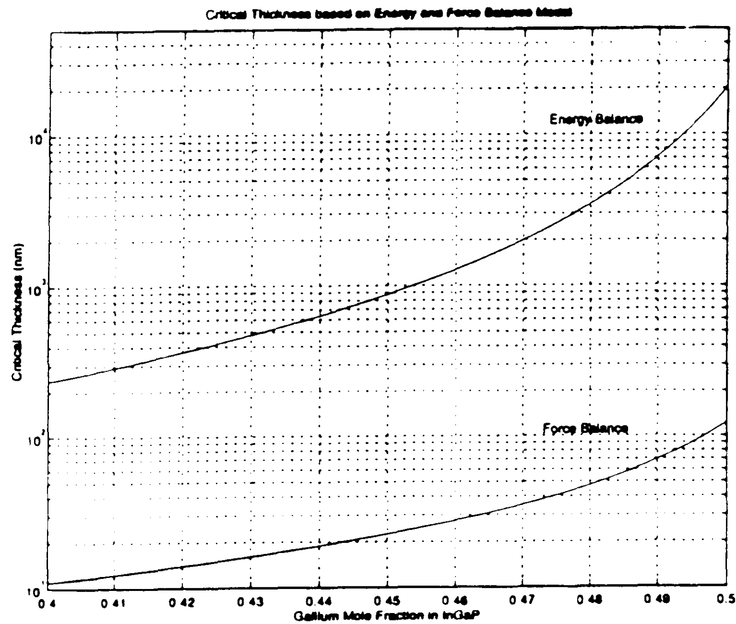

Figure 3-3: The critical thickness versus composition x in $In_{1-x}Ga_xP$ calculated from the force-balancing model and the energy-balancing model.

from the force-balancing model, and is much closer to the experimental value as discussed below.

3.3 Discussion

In the previous two sections, two models were introduced to calculate the critical thickness. The critical thickness versus composition x for $In_{1-x}Ga_xP$ on a GaAs substrate based on the force-balancing model and the energy-balancing model are shown in Fig. 3.3. The critical thickness from the energy-balancing model is found to be significantly larger than that of the force-balancing model and is very close to the experimental data of (In,Ga)P grown by GSMBE on GaAs. A larger critical thickness suggests that the misfit strain in the film is difficult to be relaxed such that the strain is no longer accommodated elastically. The formation of misfit dislocations to relieve the misfit strain is more difficult.

By examining the history of the Matthews and Blakeslee's theory, it was proposed in 1970s and is based on the experimental results obtained from liquid phase epitaxy (LPE). Here the existence of grown-in threading dislocations was assumed. The model was based on balancing the force exerted by misfit stress on a threading dislocation and the tension in the dislocation line. Therefore, Matthews-Blakeslee's model will not be valid if the film is grown on a high quality substrate in a layer-by-layer growth (such as occurs in MBE) where the misfit strain is relatively small and very few threading dislocations exist in the film at the initial stage of the growth. However, in the LPE-grown film, due to the limitation of the growth mechanism (3D-growth), there are many more threading dislocations which exist in the epitaxial layer and the threading dislocations play a significant role in the relief of the misfit strain.

On the other hand, the energy-balancing model does not assume the existence of threading dislocations. It assumes that the film is grown on a very high quality substrate, where the initial growth mechanism is layer-by-layer. At the start of the growth, there are only isolated screw dislocations existing in the film. The interfacial misfit dislocations are generated when the areal strain energy density of the film exceeds the self-energy of an isolated screw dislocation. Because of the absence of the threading dislocations, this model applies to the high quality (In,Ga)P films grown here and has a much higher critical thickness than the force-balancing model.

In the case of (In,Ga)P films, a sharp 2×1 RHEED reconstruction pattern is observed at the beginning of the growth. The sharp RHEED pattern suggests good surface microstructure. RHEED intensity oscillations measured at the beginning of the growth last more than 6 minutes. The observation of the long RHEED intensity oscillations also indicates a near perfect layer-by-layer growth mode at the beginning of the growth. The quality of the film during the initial growth is very high and there are very few threading dislocations in the film. Therefore, the assumption of grown-in threading dislocations will be invalid and the energy-balancing model will be more appropriate to evaluate the critical thickness.

On the other hand, at the beginning of ZnSe nucleation on a GaAs substrate, the RHEED pattern is very diffusive. Arrow head-like RHEED patterns are often

observed. This phenomenon suggests that the nucleation is not in a layer-by-layer growth mode. The microstructure of the surface is rough during the initial growth stage and can introduce a large number of threading dislocations. Dense threading dislocations are commonly observed near the interface between ZnSe and the GaAs substrate using TEM. The presence of massive threading dislocations near the epitaxial layer interface indicates that the force-balancing model are more appropriate in determining the critical thickness of ZnSe grown on GaAs substrates. The lattice-mismatch between ZnSe and GaAs is 0.25%. Using Eq. 3.3, a critical thickness of 1500 Å is obtained. This value is consistent with the experimental value of 150 nm [19].

Our experiments also find that the tensile strain in the epitaxial layer is relaxed more easily than the compressive strain. The energy-balancing model can not explain this phenomenon. The critical thickness calculated from energy-balancing model is the same for the same amount of tensile or compressive strain (Fig. 3-4). We speculate that this is because in the energy-balancing model, only the areal energy density of a screw dislocation is calculated. But the tensile film and compressive film might use two different kinds of isolated dislocation to relax the strain. Further study is needed to clarify this phenomenon.

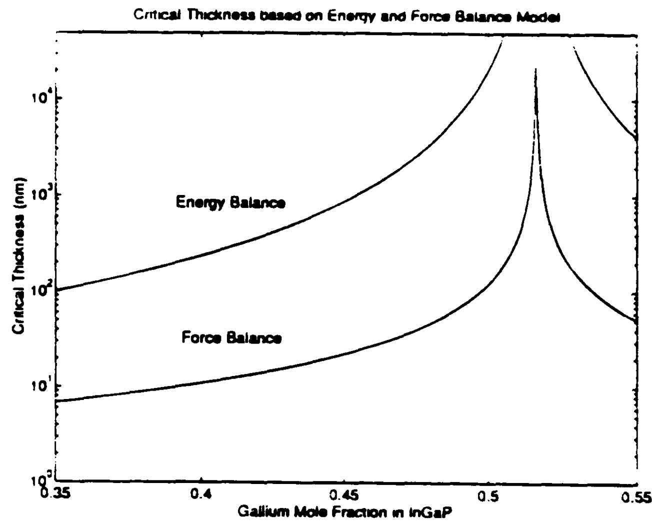

Figure 3-4: The critical thickness under tensile and compressive strain evaluated from energy-balancing model.

Chapter 4

X-ray Characterization

A High Resolution Double Crystal X-ray Diffraction (HRXRD) measurement is a powerful tool to measure the lattice-mismatch between an epitaxial layer and the substrate and for assessing crystal quality. The simple mechanism behind x-ray diffraction is illustrated in Fig. 4-1. If the wavelength of a x-ray beam is λ, and the distance between the two lattice planes is a, then a diffracted x-ray peak intensity will be detected at an angle θ that satisfies

$$2a \sin\theta = \lambda/2. \tag{4.1}$$

If the x-ray beam is ideal with no wavelength dispersion, then the full-width-at-half-maximum (FWHM) of the diffracted beam is a very good indicator for the crystal quality. For a high quality semiconductor crystal grown by MBE or GSMBE, the FWHM of the x-ray rocking curve is on the order of 10 arcseconds [39]. However, all x-ray sources produce radiation covering a finite wavelength range and with some finite divergence. For a single crystal x-ray diffraction measurement, the magnitude of instrumental broadening of the diffracted beam is too large to acquire any reasonable assessment of the reflection width of high quality crystals. The instrumental line width broadening is eliminated by employing the double crystal x-ray diffraction geometry. After the x-ray beam is reflected from the first crystal, the wavelength components are separated in space (Fig. 4-2). Therefore, the x-ray beams with different wavelengths

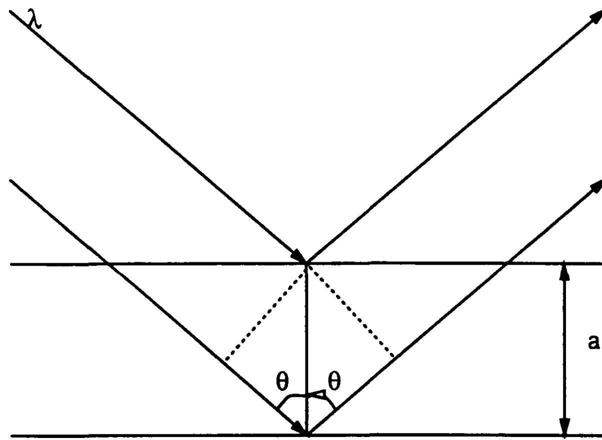

Figure 4-1: Schematic illustration of the x-ray diffraction mechanism

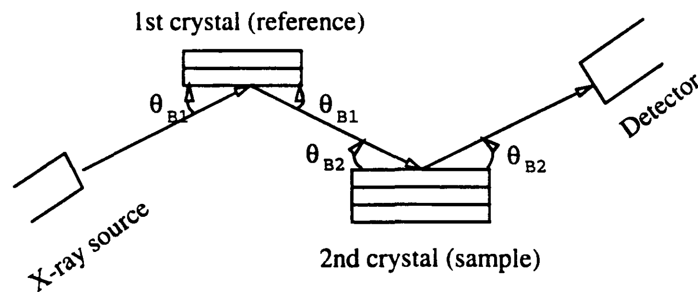

Figure 4-2: Schematic illustration of a double crystal x-ray diffraction measurement setup

are incident onto different parts of the sample. It is possible to shield most of the undesired wavelengths from the sample. Most modern day structural characterization techniques for high quality semiconductor thin films are done by double crystal x-ray diffraction measurements. A detailed description of HRXRD will be given in the following sections.

4.1 Structural Characterization of (In,Ga)P

For a fully relaxed, plastically deformed zincblende semiconductor thin film on a (100)-oriented substrate, the out-of-plane lattice constant $a_\perp$ should be equal to the in-plane lattice constant $a_{||}$. The lattice constant of the material can be very easily found by performing the (400) x-ray diffraction measurement. In this case, the diffraction angle satisfies

$$2\frac{a}{2}\sin\theta = \frac{\lambda}{2} \tag{4.2}$$

where λ is the x-ray wavelength. The lattice constant for the substrate material is usually known, and the substrate is totally relaxed or unstrained. a_{sub} is equal to $\frac{\lambda}{2}\sin\theta_B$ where θ_B is the Bragg angle for the substrate material. The out-of-plane lattice constant, $a_\perp$, of the epitaxial layer is

$$a_\perp = \frac{\lambda}{2}\sin(\theta_B + \Delta\theta) \tag{4.3}$$

where $\Delta\theta$ is the angular separation between the epitaxial layer peak and the substrate peak. Combining Eq. 4.2 and Eq. 4.3,

$$a_\perp = a_{sub}\frac{\sin\theta_B}{\sin(\theta_B + \Delta\theta)}. \tag{4.4}$$

is obtained.

If the epitaxial layer is tilted with respect to the substrate (Fig. 4-3), then two rocking curves are needed to obtain $a_{||}$. A common method is to measure the second rocking curve with the sample rotated azimuthally by 180 degrees, then the two rocking curves will yield

$$\Delta\omega_1 = \Delta\theta + \Delta\Phi \tag{4.5}$$

$$\Delta\omega_2 = \Delta\theta - \Delta\Phi \tag{4.6}$$

where $\Delta\Phi$ is the tilt angle between the epitaxial layer and the substrate. $\Delta\omega$ is the relative sample rocking angle. From Eq. 4.5 and Eq. 4.6, $\Delta\theta = (\Delta\omega_1 + \Delta\omega_2)/2$ can be obtained.

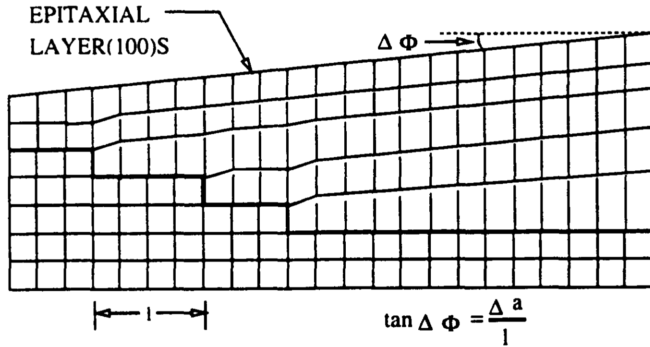

Figure 4-3: Schematic illustration of the tilt which develops for a mismatched and tetragonally-distorted coherent epitaxial layer grown on a stepped surface

For most epitaxial layers lattice-mismatched to the substrate, unless the layer is sufficiently thick that the lattice is totally relaxed, the epitaxial layer will not have the same cubic unit cell as that of the substrate. It will be tetragonally distorted by the lattice-mismatch stress originating from the substrate lattice. The lattice parameter $a_{||}$ in the growth plane will be different from the lattice parameter $a_{\perp}$ in the growth direction. For most semiconductor materials, misfit is accommodated by misfit dislocations. By calculating the stress in the layer and in the substrate, the relationship between the a_r which is the relaxed mismatch in the absence of coherent strain, $a_{||}$ and $a_{\perp}$ are found to be

$$\left[\frac{a_r - a}{a}\right] = \frac{1-\nu}{1+\nu}\left[\frac{a_{\perp} - a}{a}\right] + \frac{2\nu}{1+\nu}\left[\frac{a_{||} - a}{a}\right] \tag{4.7}$$

where ν is the Poisson ratio, and a is the substrate lattice constant. The alloy composition is then obtained from the relaxed lattice constant by Vegard's law.

(400) x-ray diffraction can only measure the lattice parameter along the growth direction. In order to measure the in-plane lattice constant, asymmetric reflections from lattice planes that are not perpendicular to the growth direction are used [40]. Consider a general (hkl) reflection which is asymmetric (Fig. 4-4). Bragg's law for

the substrate is

$$\lambda = \frac{2a_s \sin\theta_B}{\sqrt{h^2+k^2+l^2}} \tag{4.8}$$

For the epitaxial layer, the Bragg angle is written as $\theta_B + \Delta\theta$ and

$$\lambda = 2\sin(\theta_B + \Delta\theta)\left[\frac{h^2+k^2}{a_{\|}^2} + \frac{l^2}{a_{\perp}^2}\right]^{-1/2} \tag{4.9}$$

where l is taken to be the index along the growth direction (the direction that is perpendicular to the substrate surface). If Φ is defined as the angle between the normals to (hkl) planes of the substrate and the growth direction, $\Phi + \Delta\Phi$ as the angle between the the normals to (hkl) planes of the epitaxial layer and the growth direction, θ_B as the Bragg angle, then the relationships between Φ and (hkl) are

$$\cos\Phi = \frac{1}{\sqrt{h^2+k^2+l^2}}; \tag{4.10}$$

$$\sin\Phi = \frac{h}{\sqrt{h^2+k^2+l^2}}; \tag{4.11}$$

$$\cos(\Phi + \Delta\Phi) = \frac{\frac{l}{a_\perp}}{\sqrt{\frac{h^2+k^2}{a_{\|}^2} + \frac{l^2}{a_\perp^2}}}; \tag{4.12}$$

and

$$\sin(\Phi + \Delta\Phi) = \frac{\frac{h}{a_{\|}}}{\sqrt{\frac{h^2+k^2}{a_{\|}^2} + \frac{l^2}{a_\perp^2}}}. \tag{4.13}$$

We can further simplify Eq. 4.8 and Eq. 4.9

$$\Delta\theta_B = \left[-\left(\frac{\Delta a}{a}\right)_\perp \cos^2\Phi + \left(\frac{\Delta a}{a}\right)_{\|} \sin^2\Phi\right]\tan\theta_B; \tag{4.14}$$

$$\Delta\Phi = \left[\left(\frac{\Delta a}{a}\right)_\perp - \left(\frac{\Delta a}{a}\right)_{\|}\right]\sin\Phi\cos\Phi. \tag{4.15}$$

The x-ray rocking curve peak separation $\Delta\theta$ between the substrate and epitaxial layer is

$$\Delta\theta = \Delta\theta_a + \Delta\Phi \tag{4.16}$$

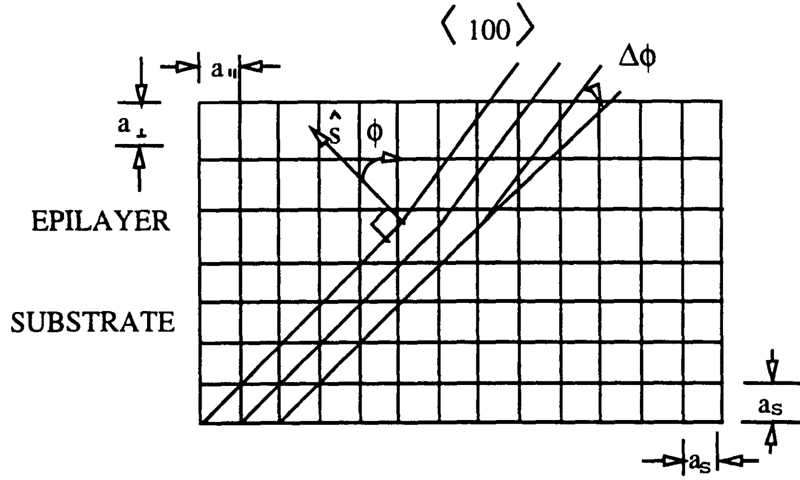

Figure 4-4: The misorientation angle between epitaxial layer and substrate Bragg planes for the case of a coherent and tetragonally distorted epitaxial layer.

for glancing incidence and

$$\Delta\theta = \Delta\theta_B - \Delta\Phi \tag{4.17}$$

for glancing exit as illustrated in Fig 4-5.

From equations 4.15, 4.16, and 4.17,

$$\Delta\theta = \left(\frac{\Delta a}{a}\right)_{||}(-\sin^2\Phi\tan\theta_B + \Phi\cos\Phi) + \left(\frac{\Delta a}{a}\right)_{\perp}(-\cos^2\Phi\tan\theta_B - \sin\Phi\cos\Phi) \tag{4.18}$$

for glancing incidence and

$$\Delta\theta = \left(\frac{\Delta a}{a}\right)_{||}(-\sin^2\Phi\tan\theta_B - \sin\Phi\cos\Phi) + \left(\frac{\Delta a}{a}\right)_{\perp}(-\cos^2\Phi\tan\theta_B + \sin\Phi\cos\Phi) \tag{4.19}$$

for glancing exit.

From the above equations, it is easy to see that two measurements are required to obtain both $a_\perp$ and $a_{||}$ of the epitaxial layer. In practice it is convenient to measure both the glancing-incidence and glancing exit reflections. However, for the equipment on which no glancing exit reflection is available, $a_\perp$ by (400) x-ray diffraction and $a_{||}$ can be obtained from asymmetric glancing incidence measurements.

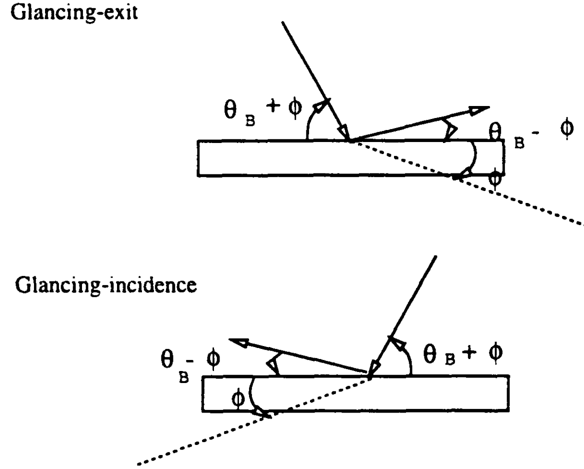

Figure 4-5: Glancing exit and glancing incidence for an asymmetric x-ray reflection.

A Bede model 200 two-crystal x-ray system using Cu-Kα radiation is used in this study. The first crystal is InP oriented for the (400) reflection. Rocking curves are measured for symmetric (400) as well as asymmetric (511) reflections off the second crystal (Fig. 4-6). The spot size of the x-ray beam on the sample is approximately 1 mm by 2 mm [41]. Data points are typically collected every 2 arcseconds with a count time of 2 seconds per point. For some very thin films whose thickness are below 1000 Å, a count time of 5 to 10 seconds is used because of the low relative intensity ratio of the film peak to substrate peak.

Fig. 4-7 shows a typical (400) x-ray rocking curve. The sample consists of a 1 μm (In,Ga)P layer grown on a GaAs substrate. Because the symmetric (400) reflection geometry is used, the $a_\perp$ of the (In,Ga)P is found using Eq. 4.3. Without knowledge of the absolute angle of the (In,Ga)P peak, the absolute angle for the GaAs peak has to be determined first. The GaAs lattice constant is 5.6532$\AA$. The Cu-Kα_1 x-ray line has a wavelength of 1.54056Å. Using Eq. 4.3, the absolute angle of the GaAs peak is 33.01^o for the (004) GaAs Bragg angle. The separation between the peaks, $\Delta\theta$, is +328 arcseconds. Again using Eq. 4.3, $a_\perp$ of (In,Ga)P is 5.6394Å. If the (In,Ga)P is further assumed to be pseudomorphic to the GaAs substrate ($a_{||} = a_{GaAs}$), the Ga mole fraction of (In,Ga)P is obtained by using Eq. 4.8. The Poisson ratio is 0.360 for

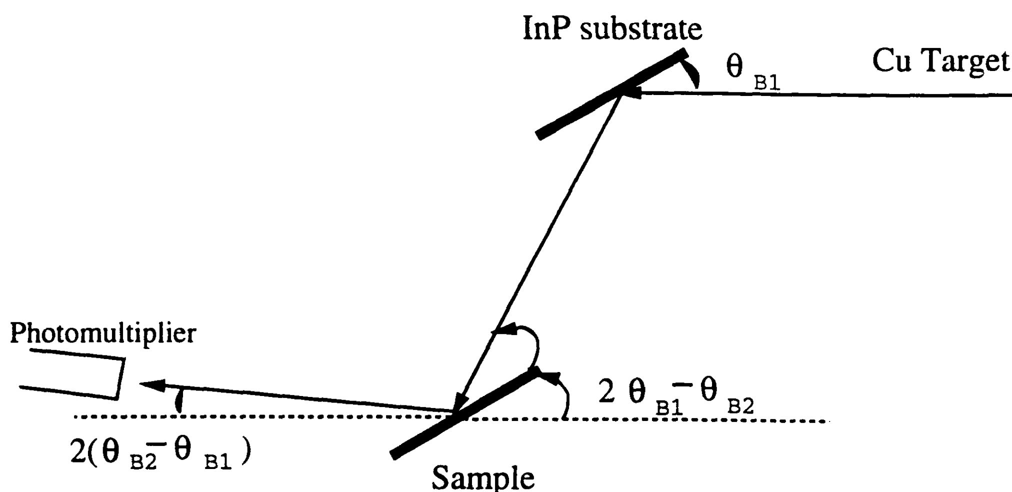

Figure 4-6: Bede x-ray setup and the relationships between the angles of first crystal, second crystal and the detector.

InP, 0.307 for GaP. The Ga composition of (In,Ga)P is known to be approximately 50% from the growth. To the first order, by using Vegard's law, the Poisson ratio is 0.333. The Ga composition of (In,Ga)P is 53.3%.

For an (In,Ga)P layer lattice-mismatched to the GaAs substrate, if the thickness is larger than the critical thickness, misfit dislocations will be introduced to relieve the strain. The (In,Ga)P epitaxial layer will no longer be pseudomorphic to the substrate. Unless the film is totally relaxed, $a_\perp$ will not be equal to $a_{||}$. (511) asymmetric reflection geometry is necessary to measure the in-plane lattice constant $a_{||}$. A typical HRXRD scan is shown in Fig. 4-8. The sample consists of a 4 μm (In,Ga)P layer on a GaAs substrate. Cross hatching is observed on the epitaxial layer surface, which indicates the film is at least partially relaxed (Fig. 4-9). The out-of-plane lattice constant $a_\perp$ is 5.6952 $\AA$ by using the (400) x-ray rocking curve. The (511) rocking curve is measured by changing the detector position and the x-ray sample holder stage positions.

Using Eq. 4.8, the (511) Bragg angle θ_B is 45.07°. The angle between (511) planes and (400) planes is 15.793°. If glancing incidence is chosen, the x-ray should be incident at 29.3° above the horizontal plane. The (400) GaAs Bragg angle is chosen

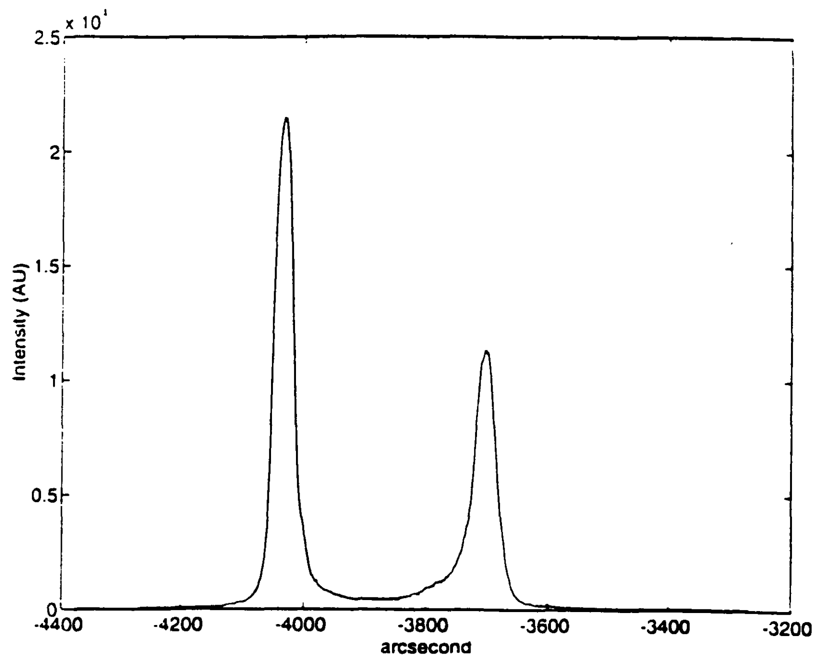

Figure 4-7: A typical (400) double crystal x-ray diffraction rocking curve for a 1 μm pseudomorphic (In,Ga)P layer on the GaAs substrate. The peak separation between (In,Ga)P and GaAs is 328 arcseconds.

as the reference. The x-ray sample holder stage is rotated 4° clockwise from the (400) GaAs peak. The detector is also rotated anti-clockwise by 60.8^o above the horizontal plane. For this particular sample, the (511) x-ray rocking curve peak separation between the (In,Ga)P and GaAs is found to be -1710 arcseconds. Since $a_\perp$ is 5.6952, using Eq. 4.18, $(\Delta a/a)_{||}$ is found to be 0.25%, and $a_{||}$ is 5.667. From Eq. 4.8, $\Delta a/a$ is found to be 0.49%. The Ga composition is obtained to be 45%. Even for a film which is 4 μm thick having a lattice-mismatch of 0.49% when fully relaxed, it is still found to be only 50% relaxed.

4.2 X-ray Diffraction Measurement of (In,Ga)P Buffer Layer

In order to determine the composition of the (In,Ga)P buffer layers, as well as the strain and crystal quality of the film, extensive x-ray diffraction measurements have been performed on the samples. The first group of samples examined is the (In,Ga)P films having Ga composition varying from 44% to 55% and thicknesses of 1 μm. Most

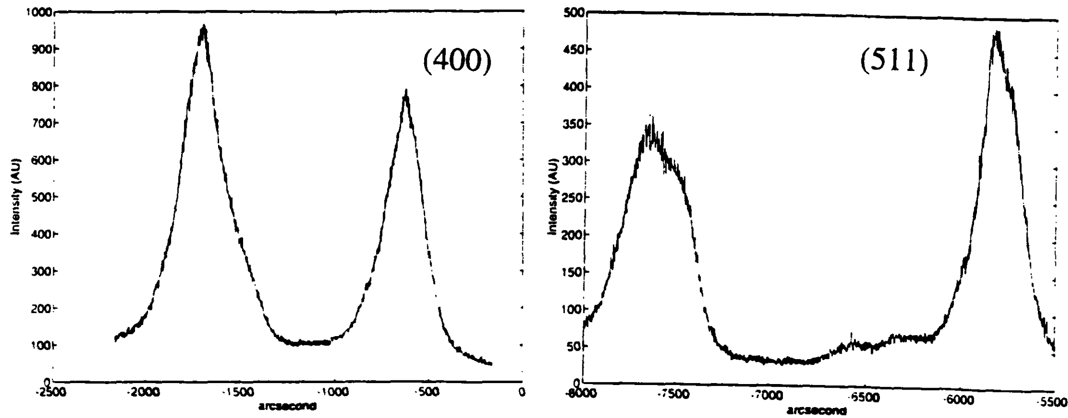

Figure 4-8: The (400) and (511) double crystal x-ray diffraction rocking curves for a partially-relaxed (In,Ga)P film.

of the samples in this group are pseudomorphic to the GaAs substrate as indicated by (511) x-ray diffraction measurements. Fig. 4-10 is the (400) double crystal x-ray diffraction rocking curve for sample InGaP 28. For this sample, the GaAs peak has a FWHM of 26 arcseconds. The (In,Ga)P peak has a FWHM of 34 arcseconds. The Ga composition is obtained to be 46% by using Eq. 4.7. Fig. 4-11 is the (400) x-ray rocking curve for sample InGaP 117. From the angular separation of (In,Ga)P and GaAs peaks, the Ga composition of this film is 51% and is almost lattice-matched to the GaAs substrate. The FWHM of (In,Ga)P peak is 18 arcseconds, while the FWHM of GaAs substrate peak is 14 arcseconds. Although both samples have different mole compositions, their x-ray rocking curve FWHM are similar. The surface morphology of the films is featureless and mirror-like. The narrow x-ray rocking curve FWHM and good surface morphology indicate the high structure quality of the (In,Ga)P buffer layers grown for this investigation. The high crystal quality, i.e., the absence of threading dislocations present in the films, and the pseudomorphic nature of the films further provides evidence that the energy-balancing model is the appropriate model to evaluate the critical thickness.

The second group of samples examined are all 4 μm thick with Ga composition varying from 43% to 52%. As shown in Fig. 4-12, with an increase in the lattice-mismatch with the GaAs substrate, the FWHM of the (In,Ga)P peak increases significantly from 30 arcseconds to 300 arcseconds. From (511) and (400) x-ray rocking curves, it is found that the strained (In,Ga)P film starts to relax as the Ga compo-

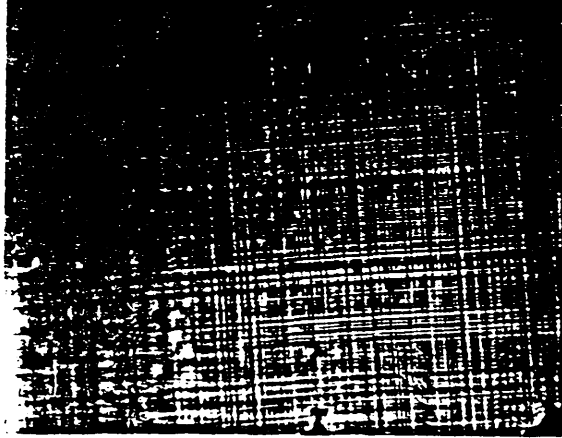

Figure 4-9: Interference optical micrograph of a partially-relaxed (In,Ga)P on GaAs substrate showed cross hatching patterns along [100] and [010] directions

sition is increased (Fig. 4-13). These data support the energy-balancing model that predicts that the critical thickness of (In,Ga)P is around 3 μm. The broadening of the x-ray rocking curve for the partially-relaxed films is due to the introduction of misfit dislocations. When a film is pseudomorphic to the substrate, the strain accommodates the lattice misfit between substrate and (In,Ga)P buffer layer. However, when (In,Ga)P is partially or completely relaxed, misfit dislocations are introduced to relieve the strain between GaAs and (In,Ga)P. These misfit dislocations will act as scattering centers reducing the intensity of (In,Ga)P x-ray peak and broadening the FWHM. For the relaxed films, significant cross hatching was observed on the surface. It is well known that cross hatching is formed when the misfit dislocations are bent into [010] and $[0\bar{1}0]$ directions. The formation of the cross hatching often means a reduction of threading dislocations, which is highly desirable in our case. The nature of lattice mismatch between ZnSe and GaAs determines that misfit dislocations have to exist somewhere inside the relaxed ZnSe/III-V heterostructure grown

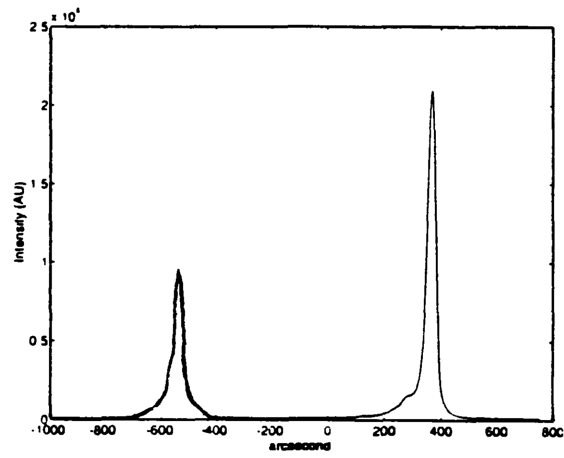

Figure 4-10: The (400) double crystal x-ray diffraction rocking curve of (In,Ga)P having a FWHM of 34 arcseconds.

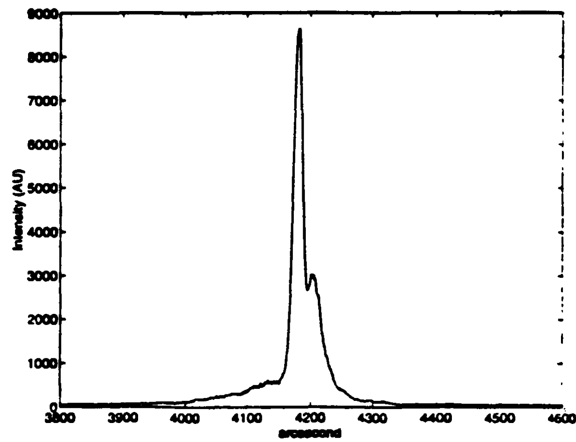

Figure 4-11: The (400) double crystal x-ray diffraction rocking curve of (In,Ga)P having a FWHM of 18 arcseconds.

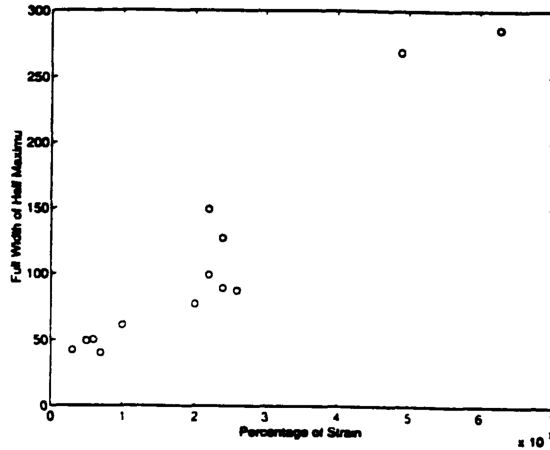

Figure 4-12: FWHM of (In,Ga)P x-ray rocking curves versus lattice mismatch between (In,Ga)P and GaAs substrate.

on GaAs substrate. If the dislocations are created near the interface of GaAs and (In,Ga)P layers, and these dislocations are subsequently bent into (010) and $(0\bar{1}0)$ direction, then the isolation of misfit dislocations is achieved. The subsequent ZnSe and (In,Ga)P interface will be free of dislocations.

The surprising phenomena observed is that the FWHM of GaAs substrate also increases with the increase of the FWHM of (In,Ga)P film. Similar phenomenon has also been observed in $In_{0.04}Ga_{0.96}As$ on the GaAs substrate [42]. The broadening of GaAs x-ray rocking curve peak is believed to be caused by the misfit dislocation propagating back towards the substrate.

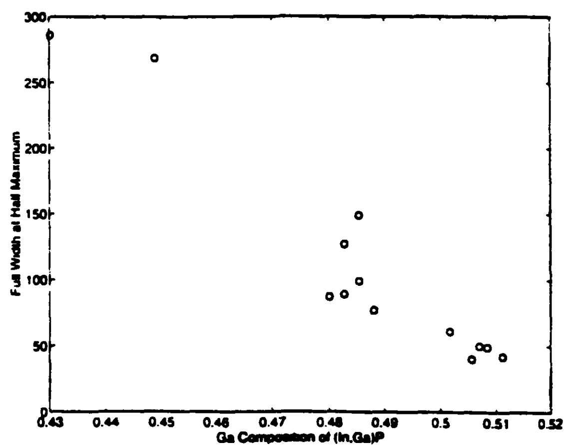

Figure 4-13: (In,Ga)P lattice relaxation versus Ga composition for (In,Ga)P epitaxial layers

Chapter 5

Structural and Optical Characterization of ZnSe on (In,Ga)P

ZnSe epitaxial layers have been grown on strained 1 μm (In,Ga)P and partially-relaxed 4 μm (In,Ga)P buffer layers. As discussed in Chapter 4, films of (In,Ga)P having 1 μm thickness are pseudomorphic to the GaAs substrate. Fig. 5-1 shows the (400) rocking curve obtained from the ZnSe/(In,Ga)P/GaAs heterostructure containing a 1.9 μm ZnSe and a 1.15 μm $In_{0.5}Ga_{0.5}P$ buffer layer. Fig. 5-2 shows the identical structure following the removal of the 1.9 μm ZnSe layer by selective etching. In this case, the ZnSe exhibits a FWHM of 130 arcseconds, whereas the (In,Ga)P buffer layer exhibits a FWHM of 18 arcseconds. A 1.1 μm ZnSe film on a 4.3 μm (In,Ga)P buffer layer (having a FWHM of 35 arcseconds) exhibited a larger FWHM ($\sim$ 200 arcseconds). The Ga composition of the (In,Ga)P buffer layer for this structure is 48% such that when it is fully relaxed, the in-plane lattice constant would be the same as that of ZnSe. For this structure, the (511) rocking curves indicate that the 4 μm (In,Ga)P is not fully relaxed, but still contained approximately 0.11% mismatch between the ZnSe and the (In,Ga)P.

The FWHM of the x-ray rocking curve reflects the presence of dislocations at the ZnSe/III-V heterointerface due to the presence of the lattice-mismatch. Large

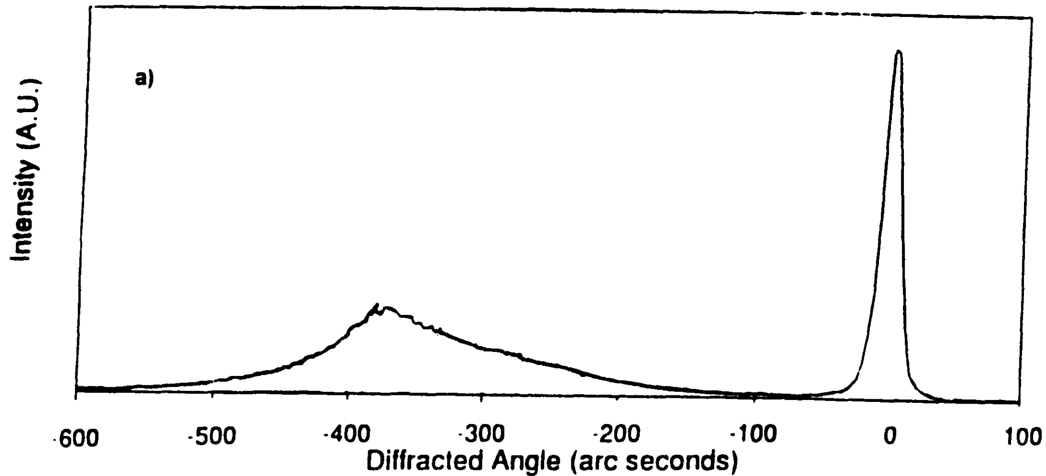

Figure 5-1: The (400) rocking curve of 1.9 μm ZnSe/1.15 μm $In_{0.5}Ga_{0.5}P$/GaAs heterostructure. The FWHM of the ZnSe is 130 arcseconds.

FWHM of the ZnSe epitaxial layers grown on (In,Ga)P buffer layers indicates that the ZnSe films are relaxed and misfit dislocations and threading dislocations are present in the film. TEM confirms that a large number of threading dislocations exist near the interface between ZnSe and (In,Ga)P buffer layers, while fewer dislocations are observed in the areas that are further away from the interface (Fig. 5-3). This explains why the 1.15 μm ZnSe/4 μm (In,Ga)P exhibits a larger x-ray FWHM than the 2 μm ZnSe/1 μm (In,Ga)P. From the TEM images, both of the films have similar dislocations densities near the interface. These threading dislocations contribute more to the broadening of the thin epitaxial layers's x-ray peak than the thick layers'. Therefore, the FWHM of the 2 μm ZnSe is smaller than that of the 1 μm ZnSe.

An interesting comparison is made between the relaxed ZnSe and the relaxed (In,Ga)P. Fig. 5-5 is a (400) x-ray rocking curve of a 4 μm partially-relaxed $In_{0.56}Ga_{0.44}P$ on GaAs substrate. The FWHM is 230 arcseconds which is much larger than that of relaxed ZnSe (FWHM of 130 arcsecond) on GaAs substrate. From the larger FWHM, it is expected that a large number of dislocations will be present in the (In,Ga)P. However, (In,Ga)P TEM images show no dislocations present on the scale of 500$\AA$ (Fig. 5-4). Instead, cross-hatched surface is observed under the microscope. On the contrary, ZnSe has a smaller x-ray FWHM, but a much larger number of

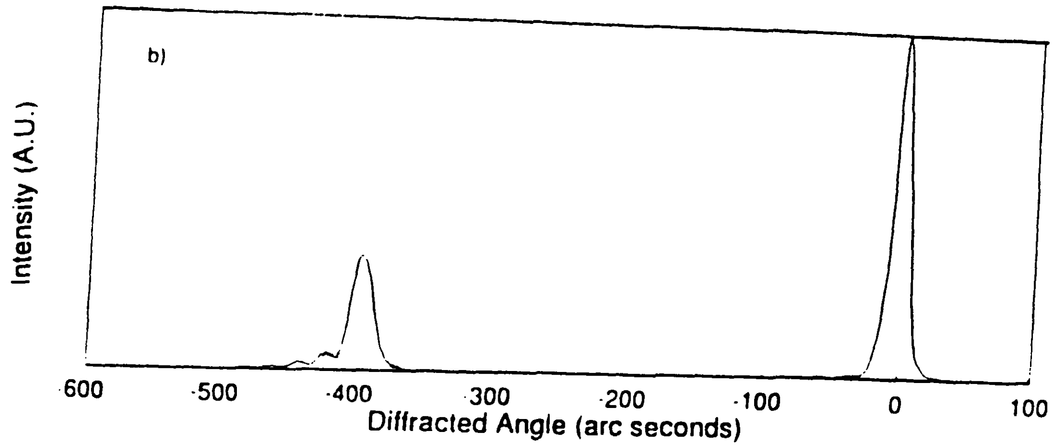

Figure 5-2: The (400) rocking curve of the 1.15 μm $In_{0.5}Ga_{0.5}P$ heterostructure having a FWHM of 18 arcseconds.

Figure 5-3: TEM image of 2 μm ZnSe/1 μm (In,Ga)P heterostructure [36].

Figure 5-4: TEM image of the interface between 4 μm $In_{0.56}Ga_{0.44}P$ and the GaAs substrate [36].

threading dislocations are observed by TEM. No visible cross-hatchings are observed under the Normarski microscope. This contradiction suggests that (In,Ga)P and ZnSe have two different lattice relaxation mechanisms. While 60° misfit dislocations (the cause of the cross-hatched surface) are the major source for the lattice relaxation of (In,Ga)P, threading dislocations generated from ZnSe/GaAs interface are the principle source for ZnSe lattice relaxation. The possible causes for the different lattice relaxation mechanisms are: the growth temperature (In,Ga)P is grown at 450-500°C, ZnSe is grown at 250-300°C), surface mobility of different elements. A detailed study is needed to further solve the problem.

The optical properties of the ZnSe films are measured using photoluminescence (PL) spectroscopy. The 10K PL spectra of the ZnSe on the pseudomorphic (In,Ga)P buffer layers are dominated by the luminescence attributed to transitions associated with donor-bound excitons, and speculated to be due to a chlorine impurity. Defect-related luminescence originating from mid-bandgap deep levels is not observed. However, the photoluminescence from ZnSe grown on the partially-relaxed (In,Ga)P buffer layers consisted of features due to both donor-bound excitons (2.795 eV) and free excitons (2.803 eV) having roughly the same intensity (Fig. 5-6). For the samples

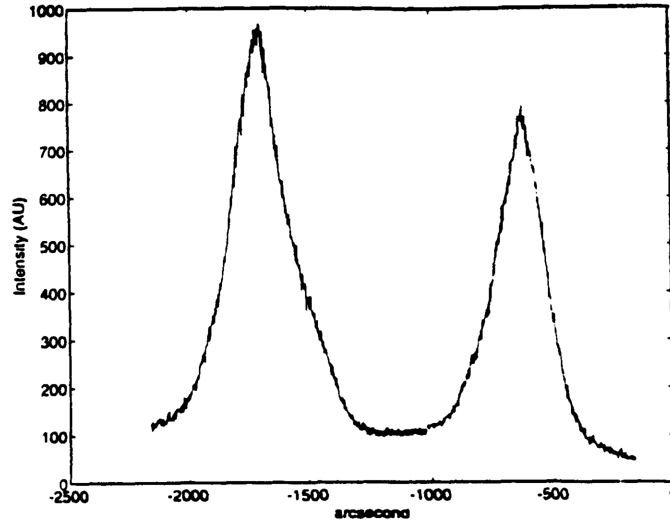

Figure 5-5: The (400) x-ray rocking curve of a 4 μm partially-relaxed (In,Ga)P on GaAs substrate

examined which have a very high degree of purity, the Y_0 and I_V transitions are typically detected. Both the Y_0 and I_V transitions have been reported to be due to extended defects [43, 44, 45] which indicated that the ZnSe layer contained defects due to lattice relaxation. The observation of the Y_0 and I_V transitions served as additional evidence that these (In,Ga)P buffer layers were only partially relaxed, whereas the ZnSe was completely relaxed. The transition occurring at 1.938 eV is attributed to the PL originating from the (In,Ga)P buffer layer.

The optical properties of (In,Ga)P are also measured using photoluminescence [46]. A typical (In,Ga)P PL data is shown in Fig. 5-7 which has a peak intensity at 1.938 eV and a FWHM of 0.01 eV. The bandgap energy, E_g, measured from PL versus Ga composition for several 4 μm thick (In,Ga)P films is plotted in Fig. 5-8. A least squares fit for this data relates the energy to the percent gallium composition as

$$E_g = 1.3067 + 0.0130 \times g \pm 0.00759eV \tag{5.1}$$

where g is the percent gallium. Using Eq. 5.1, the composition of the (In,Ga)P can be evaluated.

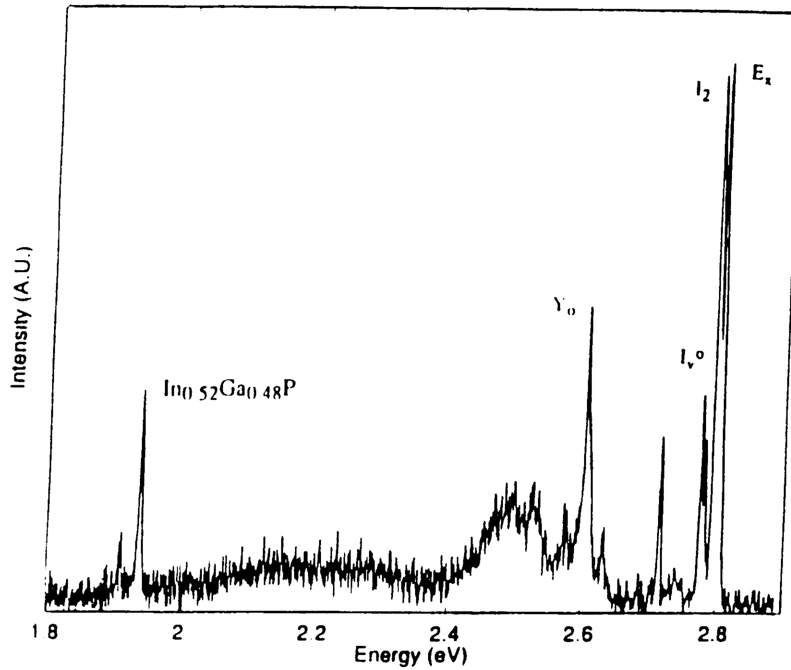

Figure 5-6: The 10K photoluminescence spectrum from a 1.1 μm ZnSe/4.3 μm $In_{0.52}Ga_{0.48}P$/GaAs heterostructure. A 0.11% lattice-mismatch still remains between the ZnSe layer and the (In,Ga)P buffer layer.

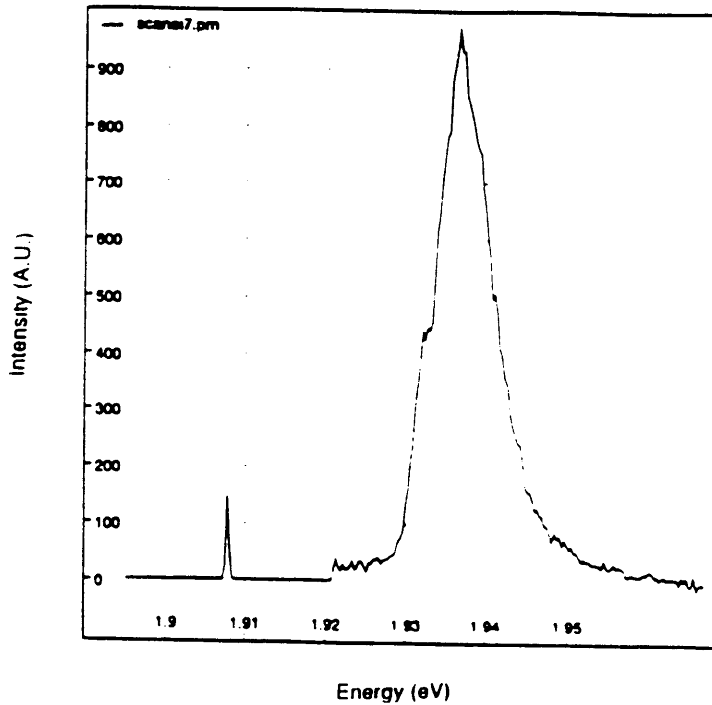

Figure 5-7: A typical PL spectrum plot for (In,Ga)P grown on the GaAs substrate.

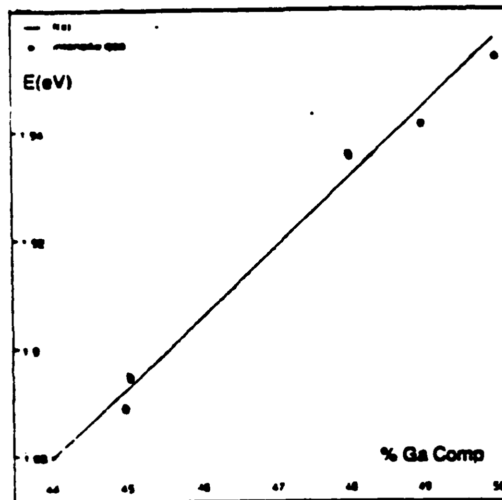

Figure 5-8: Bandgap energy versus % Ga for 4 μm (In,Ga)P films with a least square fit.

Chapter 6

Summary

In summary, high quality (In,Ga)P was grown on the GaAs substrate. The lattice relaxation behavior of the (In,Ga)P was studied. The critical thickness of the (In,Ga)P is found to be larger than that estimated by the force-balancing model. The energy-balancing model is a more accurate model to evaluate the (In,Ga)P critical thickness. High quality ZnSe films were grown on both strained and partially relaxed (In,Ga)P buffer layers. The lattice relaxation mechanism of ZnSe was found to be different from the lattice relaxation mechanism of (In,Ga)P. While the lattice relaxation of ZnSe is mainly from threading dislocations, the lattice relaxation of (In,Ga)P is introduced by 60° misfit dislocations (cross-hatching). The 10K PL spectra of the ZnSe are dominated by near bandedge features with comparable intensities of the bound and free exciton transitions, indicating a low degree of unintentional impurity incorporation.

(In,Ga)P is shown in this study to be a viable buffer layer for ZnSe and its related II-VI compounds. Further study is needed to overcome the cross-hatching appearing on the surface of the relaxed (In,Ga)P buffer layers. The detailed microstructural study of ZnSe grown on cross-hatched (In,Ga)P is also needed. Because (In,Ga)P with desired Ga mole fraction has a critical thickness of $\sim$ 3 μm, novel lattice relaxation method is needed to reduce the (In,Ga)P critical thickness. As discussed in chapter 3, misfit dislocations are the major source for the lattice relaxation. The generation of misfit dislocations depends on the growth temperature, the substrate quality, the substrate orientation, the (In,Ga)P doping concentration, and the growth method.

The critical thickness of (In,Ga)P grown on misoriented (100) GaAs substrates could be studied to determine the effect of substrate misorientation on the (In,Ga)P critical thickness.

In chapter 1, the energy band lineup of ZnSe/(In,Ga)P/GaAs is shown. p-type doped (In,Ga)P can be used to reduce the barrier to hole injection presented by the heterojunction between p-GaAs and p-ZnSe. However, a detailed (In,Ga)P electrical property study is needed. Hall mobility measurements can be used to measure the carrier mobility and the limit of the p-type doping concentration in (In,Ga)P. C-V measurements can be used to study the valence band alignment of ZnSe/(In,Ga)P/GaAs.

(In,Ga,Al)P is another possible "substrate candidate" to reduce the valence band offset between p-type ZnSe and p-type GaAs. By grading (In,Ga,Al)P from (In,Ga)P to (In,Al)P, the valence band offset between p-type ZnSe and and the p-type (In,Ga,Al)P buffer layer is reduced to 0.5 V while (In,Ga,Al)P is still lattice matched to ZnSe.

Bibliography

[1] A.Y. Cho, R.W. Dixon, Jr. H.C. Casey, and R.L. Hartman. *Appl. Phys. Lett.* 28, 501 (1976).

[2] B.I. Miller, H.H. McFee, R.J. Martin, and P.K. Tien. *Appl. Phys. Lett.* 33, 44 (1978).

[3] W.T. Tsang. *Appl. Phys. Lett.* 34, 473 (1979).

[4] W.T. Tsang and R.A. Logan. *IEEEJ. Quantum Electron.* QE_15, 451 (1979).

[5] D.L. Partin and W. Lo. *J. Appl. Phys.* 52, 1579 (1981).

[6] W.T. Tsang. *Appl. Phys. Lett.* 38, 835 (1981).

[7] W.T. Tsang, R.L. Hartman, B. Schwartz, P.E. Farley, and W.R. Holbrook. *Appl. Phys. Lett.* 39, 683 (1981).

[8] R.M. Park, H.A. Mar, and N.M. Salansky. *J. Appl. Phys.* 58 (1985) 1047.

[9] T. Mitsuyu, K. Ohkawa, and O. Yamazaki. *Appl. Phys. Lett.* 49 (1988) 1348.

[10] H. Cheng, J.M. DePuydt, J.E. Potts, and T.L. Smith. *Appl. Phys. Lett.* 52 (1988) 147.

[11] J. Ren, K.A. Bowers, B. Sneed, D.L. Driefus, J.W. Cook Jr., J.F. Schetzina, and R.M. Kolbas. *Appl. Phys. Lett.* 57 (1990) 1991.

[12] R.M. Park, M.B. Troffer, C.M. Rouleau, J.M. Depuydt, and M.A. Haase. *Appl. Phys. Lett.* 57, 2127 (1990).

[13] J. Qiu, J.M. DePuydt, H. Cheng, and M.A. Haase. *Appl. Phys. Lett.* 59, 2992 (1991).

[14] K. Ohkawa, T. Karasawa, and T. Mitsuyu. *J. Cryst. Growth.* 111, 797 (1991).

[15] M.A. Haase, J. Qiu, J.M. Depuydt, and H. Cheng. *Appl. Phys. Lett.* 59 (1991) 1272.

[16] H. Jeon, J. Ding, A.V. Nurmikko, W. Xie, D.C. Grillo, M. Kobayashi, R.L. Gunshor, G.C. Hua, and N. Otsuka. *Appl. Phys. Lett.* 60 (1992) 2045.

[17] K. Ohkawa, A. Tsujimura, S. Hayshi, S. Yoshii, and T. Mitsuyu. *Physica B.* 185 (1992) 112.

[18] S. Y. Wang, J. Simpson, H. Stewart, S.J.A. Adams, I. Hauksson, Y. Kawakami, M.R. Taghizadeh, K.A. Prior, and B.C. Cavenett. *Physica B.* 185 (1992) 508.

[19] R. Gunshor, N. Otsuka, and A. Nurmikko. *IEEE Spectrum.* May, 1993.

[20] L.H. Kuo, L. Salamanca-Riba, J.M. Depuydt, H. Cheng, and J. Qiu. *Appl. Phys. Lett.* 63, 3197 (1993).

[21] R.L. Gunshor, A.V. Nurmikko, and N. Otsuka. *Thin Solid Films.* 231 (1993) 190-196.

[22] H. Okuyama, T. Miyajima, Y. Morinaga, F. Hiei, M. Ozawa, and K. Akimoto. *Electronic Letters.* 28, (1992) 1798.

[23] F. Hiei, M. Ikeda, M. Ozawa, T. Miyajima, T. Ishibashi, and K. Akimoto. *Electron. Lett.* 29, 878 (1993).

[24] Y. Lansari, J. Ren, B. Sneed, K.A. Bowers, J.W. Cook Jr., and J.F. Schetzina. *Appl. Phys. Lett.* 61, 2554 (1992).

[25] M.A. Herman and H. Sitter. *Molecular Beam Epitaxy.* (Spriner-Verlag, New York, 1989), pp. 303-305.

[26] J. C. Vleck. *Molecular Beam Epitaxial Growth and Applications of Graded Bandgap InGaAlAs semiconducting Alloys.* MIT Ph.D Thesis (1991).

[27] C.E.C. Woodm, L. Rathbun, H. Ohno, and D. DeSimone. *J. Cryst. Growth.* 51, 299 (1981).

[28] J.C.M. Hwang, T.M. Brennan, and A.Y. Cho. *J. Electrochem. Soc.* 130, 493 (1983).

[29] M. Bafleur, A. Munoz-Yague, and A. Rocher. *J. Cryst. Growth.* 59, 531 (1982).

[30] G.M. Metze, A.R. Calawa, and J.G. Mavroides. *J. Vac. Sci. Technol.* B1, 166 (1983).

[31] E. Bauer. *Techniques of Metals research.* edited by R.F. Bunshah (1969) vol.2, pp. 501.

[32] P.K. Lorsen. *Surface Science.* (North-Hollond, Amsterdam) 169 (1986) 176-196.

[33] B.A. Joyce and J.H. Neave. *Physical Review B.* 29, 814 (1984).

[34] F.C.Frank and J.H. van der Merwe. *Proc. Roy. Soc. (London).* A 198 (1949) 216.

[35] J.W. Matthews and A.E. Blakeslee. *Journal of Crystal Growth.* 27 (1974) 118-125.

[36] TEM measurements were performed by G.C Hua and N. Otsuka at Purdue University.

[37] R. People and J.C. Bean. *Appl. Phys. Lett.* 47 (3), (1985) 322-324.

[38] F.R.N. Nabarro. *Theory of Crystal Dislocations.* (Clarendon, Oxford, 1967), p. 75.

[39] V. Swaminathan and A.T. Macrander. *Materials Aspects of GaAs and InP Based Structures.* (Prentice Hall, Englewood Cliffs, NJ, 1991).

[40] V. S. Speriosu and Jr. T. Vreeland. *J. Appl. Phys.* 56, 1591-1600 (1984).

[41] B.R. Bennett. *Molecular Beam Epitaxial Growth and Characterization of Mismatched InGaAs and InAlAs Layers on InP.* MIT Ph.D thesis.

[42] G.C Hua. private communications.

[43] J. Saraie, M. Matsumura, M. Tsubokura, K. Miyagawa, and N. Nakanura. *Jpn. J. Appl. Phys.* 28, L108 (1989).

[44] K. Shahzad, J. Petruzzello, D.J. Olego, D.A. Cammack, and J.M. Gaines. *Appl. Phys. Lett.* 57, 2452 (1990).

[45] J.O.Williams, A. Wright, and H.M. Yates. *J. Cryst. Growth.* 117, 441 (1992).

[46] J. Selph. *Characterization of InGaP Films Using Photoluminescence.* MIT 6.161 Project Report.